University of Cambridge
Department of Chemistry

Coarse-grained models
of chiral assemblies

This dissertation is submitted to the University of Cambridge
for the degree of Master of Philosophy

Scott W. Olesen

Emmanuel College

June 2012

Declaration

This dissertation is the result of my own work and includes nothing which is the outcome of work done in collaboration except where specifically indicated in the text. The contents have not previously been submitted for any degree or qualification at another institution. The number of words does not exceed 15,000.

Scott W. Olesen

June 2012

ACKNOWLEDGEMENTS

ABSTRACT

The work presented in this thesis investigates the relationship between the chirality of a building block and the chirality of structures into which these building blocks assemble. I present and use an existing single-site anisotropic coarse-grained potential for modeling the interactions between ellipsoids, and I propose a novel algorithm for computing this potential.

I introduce a building block, constructed from two sites interacting via the ellipsoidal potential, which has an adjustable chirality. The topology of the low-lying minima, which are all helical, inspired the investigation of a conformational subspace. Structures in this subspace have a well-defined and continuous chirality. A family of right-handed building blocks produces both right- and left-handed structures in this subspace, providing what I believe is the first theoretical model of this type of ambiguous relationship between building block and structure chiralities. Other building blocks constructed from these ellipsoidal sites are discussed.

Finally, I propose a single-site anisotropic potential that models a torsional interaction. Combining this single-site potential with sites interacting via the Lennard-Jones potential and an anisotropic Lennard-Jones-like potential produces membrane and ribbon structures that resemble structures observed in experiments on chiral rod-like viruses.

Glossary

Abbreviations

ECF	elliptic contact function
L-BFGS	limited memory Broyden-Fletcher-Goldfarb-Shanno
LJ	Lennard-Jones
MC	Monte Carlo
PES	potential energy surface
PY	Paramonov-Yaliraki

Contents

Chapter 1

Introduction

1.1 Coarse-grained simulations

Self-assembly, the process by which building blocks spontaneously arrange themselves into a well-ordered structure,[1] is a theme that has drawn significant attention in physics,[2] biology,[3–5] chemistry,[6] materials science,[7,8] and engineering.[9] Molecular building blocks, whose sizes are typically measured in angstroms, can be constructed using synthetic chemistry and their behavior modeled using quantum mechanical or classical atomistic potentials. Microscopic building blocks, whose sizes are typically measured in micrometers, can be modeled using classical simulations.[10] The nanoscale, or mesoscopic, regime bridges the divide between molecular and microscopic length scales.

Experiments that manipulate nanoscale objects use tools like optical tweezers,[11] atomic traps,[12] and atomic force microscopy.[13] Most of these techniques do not change the electronic structure of the objects, so there are no direct chemical changes in the manipulated materials. On the other hand, these tools rely on forces that are too weak to be used to handle macroscopic objects. Simulations treating nanoscale objects may similarly fall between previous categories. Coarse-grained potentials ignore the fine-grained details of individual atoms by grouping the simulated elements into building blocks that represent the physical building blocks relevant to the self-assembly process. This approach has the computational benefit of reducing the number of pairwise interactions that need to be computed at each simulation step.

Coarse-graining is also conceptually powerful, since it redefines the basic unit of the physical interaction. If individual atoms are indeed unimportant in a nanoscale interaction, then a theoretical model that starts at the level of the nanoscale building block should be sufficient to reproduce the appropriate behavior. Coarse-graining, then, provides information about the minimal design elements the building blocks must have in

order to reproduce observed behavior. For example, simulations have successfully modeled liquid crystal molecules as uniaxial ellipsoids[14] and rod-like colloids as spherocylinders.[15] The choices made in formulating the building blocks typically mirror choices about the level of detail that will be used to model their interactions. For example, removing solvent molecules from a simulation requires the addition of an explicit depletion force.[16,17]

1.2 Chirality

There are notable isotropic forces in nature, including gravitation, electrostatics, and the interactions between noble gas atoms.[18] Nevertheless, the anisotropy of building blocks and their interactions may be a key element in the design of the structures into which those building blocks assemble.[19,20] Using self-assembly to construct rationally designed structures and materials requires a deep understanding of the relation between the properties of the building blocks and the properties of the resultant structures.

Chiral building blocks, those that have a non-superposable mirror image, typically have chiral interactions that cause the assembled structures to be right- or left-handed.[21] The relationship between the chirality of building blocks and of the assembled structures has been treated by experiments on a variety of systems.[4,22–24] In Chapters 4 and 5 of this thesis, I use the Paramonov-Yaliraki potential[25] to model the interactions between ellipsoidal sites in two- and four-site building blocks. The two-site building blocks have a continuously adjustable chirality, and examining the chirality of a stable structure has helped clarify a single mechanism by which some of the less well-understood aspects of the relationship between the chirality of a building block and the chirality of a composite structure can be understood. In Chapter 6, I introduce a potential that itself has continuously adjustable chirality and that can be used to model the structures of clusters of rod-like viruses whose chirality can be continuously adjusted.[24]

Chapter 2

Methods

2.1 The potential energy surface

A system of N nonlinear rigid bodies has $6N$ degrees of freedom, $3N$ translational and $3N$ orientational. If a potential is associated with the system, the $6N$ variables describing the system's configuration also determine the system's energy, U. The potential energy surface (PES) is a $6N$-dimensional surface in the $(6N + 1)$-dimensional space of configurational coordinates and energy. The PES encodes all the information about the potential energy of the system's configurations.

The most interesting features of the PES are stationary points. A configuration, represented by a vector $\boldsymbol{x}$ with $6N$ components, is a stationary point on the PES if

$$\left. \frac{\partial U(\boldsymbol{x}')}{\partial x'_\alpha} \right|_{x'_\alpha = x_\alpha} = 0 \tag{2.1}$$

for all α. In one dimension, stationary points are classified as maxima, minima, or neither depending on the sign of the second derivative. In higher dimensions, there is a matrix of second derivatives, called the Hessian, H, whose entries are

$$H_{\alpha\beta}(\boldsymbol{x}) = \left. \frac{\partial^2 U(\boldsymbol{x}')}{\partial x'_\alpha \, \partial x'_\beta} \right|_{\boldsymbol{x}'=\boldsymbol{x}}. \tag{2.2}$$

A positive eigenvalue of the Hessian corresponds to the frequency of oscillation of the system along the direction in configuration space specified by the corresponding eigenvectors. Small perturbations of the system away from the stationary point along eigenvectors with positive eigenvalues will produce small oscillations. A negative Hessian eigenvalue indicates that the forces arising from U are non-restorative in the direction specified by the

corresponding eigenvectors. Perturbations along these directions will cause the system to fall away from a stationary point. The number of negative eigenvalues of the Hessian is its index. Stationary points with Hessian index zero are local minima, those with Hessian index one are transition states,[26] and those with Hessian indices greater than one are saddle points.[27]

2.2 Coarse-grained anisotropic potentials

2.2.1 Comparison of potentials

There are a number of potentials that model the interaction of anisotropic particles. Although the Gay-Berne potential[14] is the most well-known, it suffers from an opaque parameterization, does not respond well to overlapping geometries, and applies 'artificial ordering forces'.[25] Other anisotropic potentials, such as the elliptic contact potential,[28,29] use the elliptic contact function (ECF), a measure of the relative separation and orientation of two ellipsoids. Because the ECF is anisotropic at large distances, potentials based solely on the ECF are unphysical in this limit. The Paramonov-Yaliraki (PY) potential[25] avoids the artificial forces of the Gay-Berne potential by using the ECF but is also isotropic at large distances.

2.2.2 The elliptic contact function

The ECF is a scalar that characterizes the proximity of two ellipsoids. The shape and orientation of an ellipsoid is encoded in a shape matrix

$$\boldsymbol{A} = \sum_{i=1}^{3} a_i^{-2} \boldsymbol{u}_i \otimes \boldsymbol{u}_i, \tag{2.3}$$

where the $\boldsymbol{u}_i$ are orthogonal unit vectors pointing along the semiaxes of the ellipsoid, $\otimes$ is the dyadic product, and the a_i are the lengths of the semiaxes. (In a simulation, $\boldsymbol{A}$ is typically computed using $\boldsymbol{A} = \boldsymbol{R}\boldsymbol{A}'\boldsymbol{R}^T$, where $\boldsymbol{A}'$ is a diagonal matrix of the a_i^{-2} and $\boldsymbol{R}$ is a rotation matrix.) If the ellipsoid's center is at $\boldsymbol{r}$, then the ellipsoid consists of all the points $\boldsymbol{x}$ for which

$$1 = \mathcal{A}(\boldsymbol{x}) \equiv (\boldsymbol{x} - \boldsymbol{r})^T \boldsymbol{A}(\boldsymbol{x} - \boldsymbol{r}). \tag{2.4}$$

Given a second ellipsoid with quadratic form $\mathcal{B}$ and defining the object function

$$\mathcal{S}(\boldsymbol{x}, \lambda) = \lambda \mathcal{A}(\boldsymbol{x}) + (1 - \lambda)\mathcal{B}(\boldsymbol{x}), \tag{2.5}$$

the ECF is

$$F(\mathcal{A}, \mathcal{B}) = \max_{\lambda} \min_{\boldsymbol{x}} \mathcal{S}(\lambda, \boldsymbol{x}). \tag{2.6}$$

The minimization over $\boldsymbol{x}$ can be carried out analytically, as the value of $\boldsymbol{x}$ that minimizes $\mathcal{S}(\lambda, \boldsymbol{x})$ for a given λ is

$$\boldsymbol{x}(\lambda) = [\lambda \boldsymbol{A} + (1 - \lambda)\boldsymbol{B}]^{-1} [\lambda \boldsymbol{A}\boldsymbol{r} + (1 - \lambda)\boldsymbol{B}\boldsymbol{s}], \tag{2.7}$$

where $\boldsymbol{s}$ is the second ellipsoid's position. For this reason, $\mathcal{S}(\lambda, \boldsymbol{x})$ is also written as $\mathcal{S}(\lambda) \equiv \mathcal{S}(\lambda, \boldsymbol{x}(\lambda))$ so that the ECF can be reduced to a single optimization

$$F(\mathcal{A}, \mathcal{B}) = \max_{\lambda} \mathcal{S}(\lambda). \tag{2.8}$$

Although this approach is geometrically meaningful, it is simpler to compute the ECF using an equivalent formulation of the object function

$$\mathcal{S}(\lambda) = \lambda(1 - \lambda)\boldsymbol{r}_{AB}^{T} \left[(1 - \lambda)\boldsymbol{A}^{-1} + \lambda \boldsymbol{B}^{-1}\right]^{-1} \boldsymbol{r}_{AB}, \tag{2.9}$$

where $\boldsymbol{r}_{AB} = \boldsymbol{r} - \boldsymbol{s}$ is the vector separating the centers of the ellipsoids.[29] Typically the value λ_c, called the contact parameter, that minimizes $\mathcal{S}(\lambda)$ is computed using an optimization algorithm to maximize $\mathcal{S}(\lambda)$ as in equation (2.9). I present a novel method for computing the ECF in Section 3.1.

The ECF provides the scaling that will make the two ellipsoids externally tangent: the ellipsoids $\mathcal{A}(\boldsymbol{x}) = F(\mathcal{A}, \mathcal{B})$ and $\mathcal{B}(\boldsymbol{x}) = F(\mathcal{A}, \mathcal{B})$, which are rescaled versions of the original ellipsoids $\mathcal{A}(\boldsymbol{x}) = 1$ and $\mathcal{B}(\boldsymbol{x}) = 1$, meet at the contact point $\boldsymbol{x}_c = \boldsymbol{x}(\lambda_c)$. Thus,

$$F(\mathcal{A}, \mathcal{B}) = \mathcal{A}(\boldsymbol{x}_c) = \mathcal{B}(\boldsymbol{x}_c). \tag{2.10}$$

This provides a simple interpretation of the value of F: if $F = 1$, the two ellipsoids are externally tangent; if $F < 1$, the two ellipsoids overlap; and if $F > 1$, then the two ellipsoids are not in contact. Also, because $\boldsymbol{x}(0) = \boldsymbol{s}$ and $\boldsymbol{x}(1) = \boldsymbol{r}$, the value of λ_c is restricted to the interval $[0, 1]$.

The ECF provides an approximation of the distance of closest approach between two ellipsoids, which is $d = \min |\boldsymbol{x}_A - \boldsymbol{x}_B|$ subject to the constraint that $\mathcal{A}(\boldsymbol{x}_A) = \mathcal{B}(\boldsymbol{x}_B) = 1$. For $d > 0$, this distance is bounded above by the directional contact distance,

$$d_R = r_{AB} \left(1 - \frac{1}{\sqrt{F(\mathcal{A}, \mathcal{B})}}\right), \tag{2.11}$$
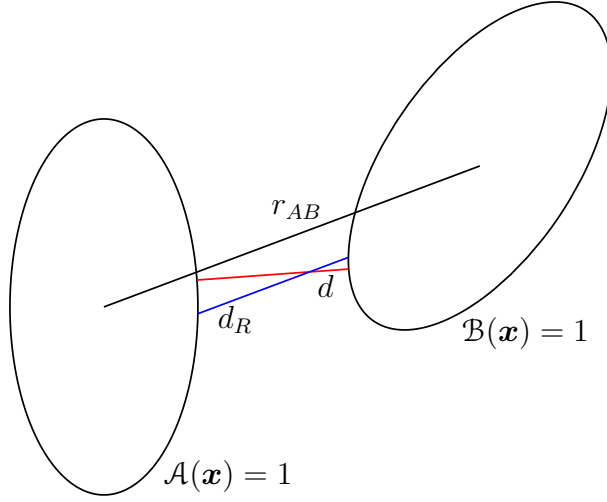
Figure 2.1: Two ellipsoids whose centers are separated by r_{AB} (black line) have a distance of closest approach d (red line) which is approximated by d_R (blue line), the distance of closest approach that is parallel to the intercenter separation.

which is the distance of closest approach between the two ellipsoids with the further constraint that $\boldsymbol{x}_A - \boldsymbol{x}_B$ must be parallel to $\boldsymbol{r} - \boldsymbol{s}$ (Figure 2.1). When two ellipsoids are in contact, both d and d_R vanish, but when the ellipsoids overlap, d remains zero while d_R becomes negative. At separations r_{AB} much larger than the ellipsoids' semiaxis lengths, the difference between the values r_{AB}, d, and d_R becomes small compared to r_{AB}.

2.2.3 The Paramonov-Yaliraki potential

Each PY site consists of two concentric ellipsoids, one repulsive and one attractive, which modulate the interactions between sites. The pairwise energy of PY sites is Lennard-Jones-like: the repulsive contribution depends on the distance of closest approach between the repulsive ellipsoids of the two sites, and the attractive contribution similarly depends on the distance between the attractive ellipsoids. The pairwise energy for two sites is

$$U = 4\epsilon_0 \left[\left(\frac{\sigma_0}{d_R^{(\mathrm{rep})} + \sigma_0} \right)^{12} - \left(\frac{\sigma_0}{d_R^{(\mathrm{att})} + \sigma_0} \right)^6 \right], \tag{2.12}$$

where ϵ_0 is an energy scale, σ_0 is a length scale, and d_R is the directional contact distance between the relevant ellipsoids. At large separations, d_R is similar to r_{AB}, so the PY potential is isotropic with respect to the orientations of the two ellipsoids in this limit.

The individual PY sites are parametrized by the shapes of the repulsive and attractive ellipsoids, which are described by the three repulsive semiaxes, a_{1i}, and the three attractive semiaxes, a_{2i}, that are used to construct the ellipsoids' shape matrices. The form of the
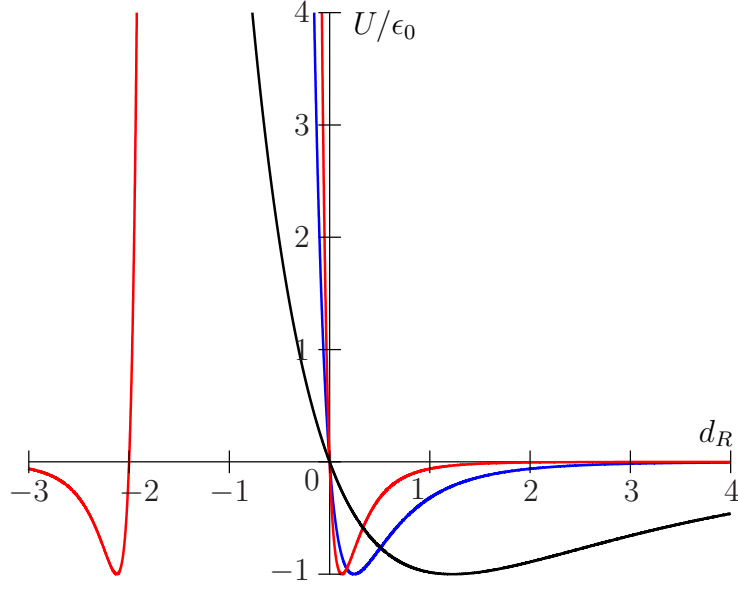
Figure 2.2: The PY potential[25] for the special case where the directional contact distances between the repulsive and attractive ellipsoids are equal. The directional contact distance d_R is in absolute units. Red line: $\sigma_0 = 1$, blue line: $\sigma_0 = 2$, black line: $\sigma_0 = 10$.

PY potential is shown in Figure 2.2 for the special case where $d_R^{(\text{rep})} = d_R^{(\text{att})}$. In this thesis, the semiaxes a_{1i} and a_{2i} are reported in absolute units. As a consequence, d_R and σ_0 are also shown in absolute units. The figure shows that as σ_0 is increased, the potential has a longer range and is softer: the external ($d_R > 0$) minimum moves further away from $d_R = 0$ and the curvature at this minimum becomes less sharp. The figure also shows the artificial internal ($d_R < 0$) minimum for $\sigma_0 = 1$. The internal minimum exists for larger σ_0, but it lies at more negative d_R. If σ_0 is sufficiently large compared to the semiaxes of the interacting ellipsoids, then d_R will never become negative enough to sample this internal minimum. A simulation can also avoid sampling this minimum by performing a check on the ECF. If $F < 1$ for some pair of ellipsoids after a change in the configuration of the system, then those two ellipsoids overlap, and that configurational change can be rejected or amended.

The richness of the PY potential is due in part to its separate parameterization of the repulsive and attractive ellipsoids. In general, the constituent ellipsoid, whether repulsive or attractive, which extends further along a given direction from the ellipsoids' common center will determine the behavior of the interaction along that direction. For example, if a site has a repulsive ellipsoid that protrudes along the equator and an attractive ellipsoid that points out at the poles, the sites will prefer to stack pole-to-pole. When a PY site is depicted in this thesis, the repulsive ellipsoid is shown.[30]

A method for cutting off the PY potential's interaction at a surface of constant po-

tential is included in Section 3.2.

2.3   Identifying minima on the PES

Choosing a potential and a system of building blocks produces a PES. Because minima lie at the 'bottom' of local areas of the PES, they are easy to find: proceeding 'downhill' from almost any point on a well-behaved PES will lead to a local minimum. This minimization, along with the attendant computation of the potentials, is typically the most computationally expensive part of a simulation that samples the PES, so it is important to use the most efficient algorithm possible.

Although there are exact solutions to certain specific minimization problems, most minimization algorithms are iterative, meaning that they produce a series of coordinates that hopefully converge to the desired minimum.[31] Iterative methods divide into three groups based on the input they require to minimize a function f. The first group of algorithms only require the function f as input. Algorithms in the second group require f and its gradient f',[32] and those in the third group require f, f', and the Hessian f''. The analytical form of the gradients of all the potentials used in this thesis are known, but algorithms involving the Hessian tend to be inefficient,[33] so all simulations here have used an iterative gradient method, the limited memory Broyden-Fletcher-Goldfarb-Shanno (L-BFGS) algorithm.[34,35] Like other quasi-Newton methods, the L-BFGS algorithm creates a sequence of approximate Hessian matrices from the function and gradient data. Our version of the algorithm uses a modified step length scaling which is more efficient than the line searches used in the original algorithm.[36] Among the gradient methods, the L-BFGS algorithm is very efficient.[37,38]

2.4   Global optimization using basin-hopping

In many applications, from finance to operations to physics, it is important to find the low-lying minima of a multivariate function.[31] In chemistry, the low-lying minima on the free energy surface will host the greatest populations when the system has equilibrated. At zero temperature, the global minima on the PES and the free energy surface coincide, so the low-lying minima on the PES provide approximate information about the structure and thermodynamics of the modeled system.[39,40] Under the right circumstances, a minimizer like the L-BFGS algorithm finds a single minimum given a single starting point. The behavior of the minimizer is purely local, so the minimizer alone is incapable of global analysis of the PES. To find global properties of the PES, most notably the identi-

ties of the low-lying minima, the minimizer must be combined with a global optimization routine.

Global optimization methods divide into two broad categories, exact and heuristic.[41] Exact, or deterministic, methods find a local minimum of the input function and produce a certificate that guarantees that this minimum is the global minimum. Because locating the global minimum on a general PES is an NP-hard problem,[42] exact methods that use no *a priori* knowledge of the PES are computationally expensive. Heuristic, or stochastic, methods produce local minima but without any guarantee that any one of these minima is the global minimum. Heuristic methods are more likely to find the global minimum if they are biased toward producing structures that include the global minimum.[41] Useful biases must be different for each system, and biasing strategies can make the global minimum more difficult to find if the strategy is formulated incorrectly. Notable unbiased heuristic global optimization methods include genetic algorithms,[43] simulated annealing,[44] taboo search,[45,46] landscape paving,[47] and deformation methods.[48,49]

All the simulations in this thesis used the basin-hopping hypersurface transformation method.[50,51] In this method, a transformed landscape $\widetilde{U}$ is obtained from the PES U by local minimization such that

$$\widetilde{U}(\boldsymbol{x}) = U\left[\text{locmin}(\boldsymbol{x})\right], \tag{2.13}$$

where $\text{locmin}(\boldsymbol{x})$ returns the coordinates of the local minimum obtained from a local minimization with starting coordinates $\boldsymbol{x}$. The energy of each point $\boldsymbol{x}$ on $\widetilde{U}$ is the energy of its local minimum $\text{locmin}(\boldsymbol{x})$ on U, so the landscape is transformed from a smooth undulating surface to a series of plateaus (Figure 2.3). If $\boldsymbol{x}$ is a local minimum on U, then $U(\boldsymbol{x}) = \widetilde{U}(\boldsymbol{x})$.

This hypersurface transformation must be combined with a global optimization method to sample the transformed surface. The simulations in this thesis were produced using a Monte Carlo[52] (MC) routine that proposes steps along the untransformed surface U and accepts or rejects the moves based on the change in energy on the transformed surface $\widetilde{U}$. The routine is:

1. Start from a local minimum $\boldsymbol{x}_n$ on U.

2. Perturb $\boldsymbol{x}_n$ to a new position $\boldsymbol{x}'$. These perturbations are designed to be unbiased and to be large enough so that $\text{locmin}(\boldsymbol{x}')$ might be distinct from $\boldsymbol{x}$.

3. If

    (a) $\widetilde{U}(\boldsymbol{x}') < \widetilde{U}(\boldsymbol{x}_n)$ or
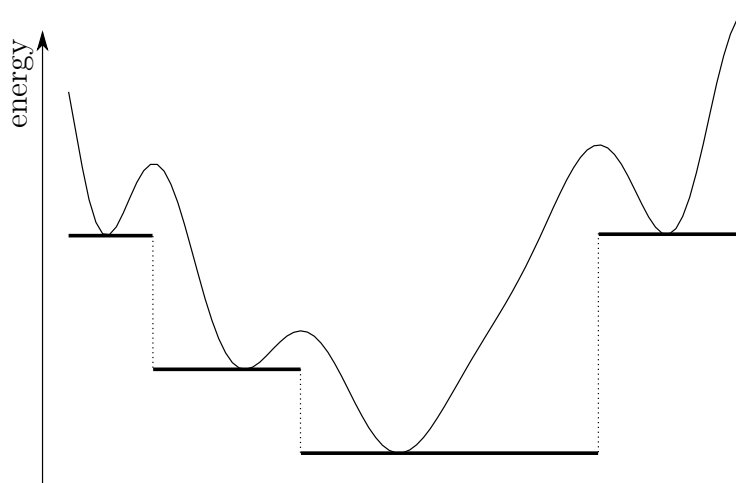
Figure 2.3: A schematic energy landscape U (thin line) and the landscape $\widetilde{U}$ (thick lines) obtained by the basin-hopping hypersurface transformation defined in equation (2.13).

(b) $\widetilde{U}(\boldsymbol{x}') > \widetilde{U}(\boldsymbol{x}_n)$ and $\exp\left\{\left[\widetilde{U}(\boldsymbol{x}_n) - \widetilde{U}(\boldsymbol{x}')\right]\Big/T\right\} > X$, where $T \geq 0$ is a temperature parameter and X is a random number drawn from the continuous uniform distribution between 0 and 1,

then accept the MC step by starting a new cycle with $\boldsymbol{x}_{n+1} \leftarrow \mathrm{locmin}(\boldsymbol{x}')$. Otherwise, reject the MC step by generating a new $\boldsymbol{x}'$ from $\boldsymbol{x}_n$.

In simulations of systems of rigid bodies, $\boldsymbol{x}'$ is produced by separately perturbing the translational and orientational parts of the coordinates of each rigid body (Figure 2.4).

The basin-hopping MC routine and all the attendant potentials used in this thesis are included in the software package GMIN.[53]

2.5   Visualizing the PES using disconnectivity graphs

It is not feasible to visualize the PES with a straightforward graph of U since the number of coordinates, $6N$, is too large. Such a graph, if it could be produced, would also not help the viewer identify low-lying minima or determine how the minima are connected. These two pieces of information can be handily combined in a disconnectivity graph.

A disconnectivity graph is produced through 'superbasin' analysis.[54] For some energy E, the minima on the PES can be grouped into superbasins. Two minima are in the same superbasin if there is a path on the PES that connects them and which never exceeds the energy E. Two minima are in different basins if every path on the PES that connects them has at least one point whose energy exceeds E. A disconnectivity graph consists of
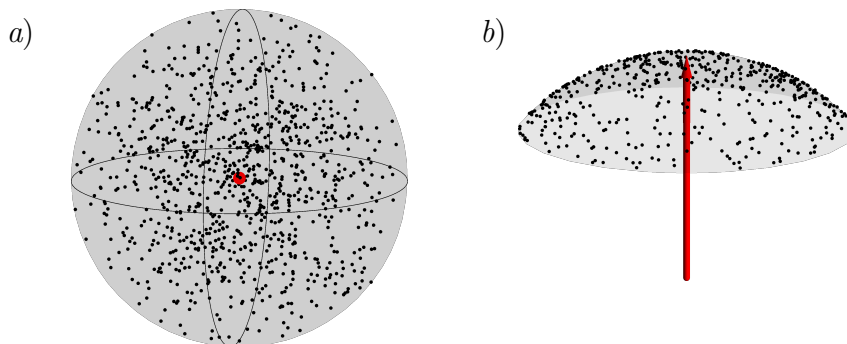
Figure 2.4: MC perturbations made to each rigid body in a simulated system. *a)* The rigid body's position (red dot) is perturbed to a new position (e.g., any one of the black dots) distributed uniformly inside a specified radius (gray sphere). *b)* The rigid body's orientation (red arrow) is perturbed to a new orientation (e.g., ending on any one of the black dots) distributed uniformly on a spherical cap (gray surface).

a series of nodes corresponding to the superbasins at a series of discrete energies E_i. A node at energy E_i is connected to a node at energy E_{i+1} if the minima in the superbasin represented by the E_i node are also in the superbasin represented by the E_{i+1} node.

If the E_i are chosen properly, the bottom of a disconnectivity graph shows individual minima on the PES. The global minimum is represented by the lowest node on that graph. If the PES has no infinite barriers, the top of the graph will consist of a single line that represents the superbasin that contains all the minima on the PES. Self-assembling systems probably have disconnectivity graphs with 'palm tree' motifs[55] (Figure 2.5). Systems with palm tree disconnectivity graphs suffer no significant traps that would prevent the system from relaxing to a global minimum relatively quickly.

The superbasin analysis as described would require exhaustive sampling of the PES, which is not computationally feasible. In practice, the disconnectivity graph is constructed using the Murrell-Laidler theorem,[26,56] which states that if two local minima have a connecting path that runs through a saddle point with index two or greater, then there is another path that runs only through transition states. The theorem also states that the maximum energy along this path is lower than the maximum energy along the original path. Thus, a disconnectivity graph can be assembled by identifying the transition states that connect pairs of minima generated during a heuristic global optimization routine. If the energies of transition states that connect two minima are each less than E, then those two minima are part of the same superbasin for E.

The routines for identifying minima and transition states and assembling them into databases are included in the software packages OPTIM[57] and PATHSAMPLE.[58]
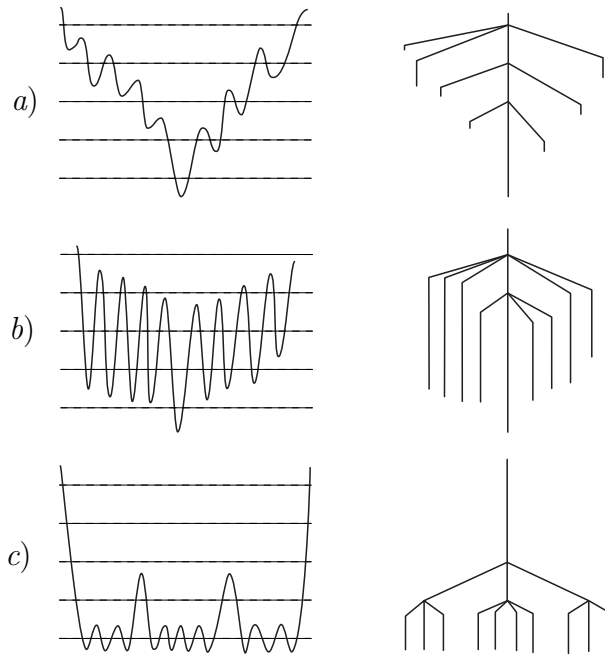
Figure 2.5: Schematic energy landscapes (left) and the corresponding disconnectivity graphs (right) produced using superbasin analysis at the energies marked by dashed lines.[27]   *a*) In a 'palm tree' motif, there are low downhill barriers toward the global minimum, which is well separated in energy from other minima. *b*) In a 'willow tree' motif, there are larger downhill barriers. *c*) In a 'banyan tree' motif, the barrier heights are much larger than the energy difference between minima, and the global minimum is not well separated in energy from other low-lying minima.

Chapter 3

Novel methods

3.1 Casting the elliptic contact function as a polynomial root-finding problem

3.1.1 Introduction

The elliptic contact function (ECF) of two ellipsoids is

$$F = \{\max \mathcal{S}(\lambda) | \lambda \in [0, 1]\}, \tag{3.1}$$

where

$$\mathcal{S}(\lambda) = \lambda(1 - \lambda)\boldsymbol{x}^T[(1 - \lambda)\boldsymbol{A} + \lambda\boldsymbol{B}]^{-1}\boldsymbol{x}, \tag{3.2}$$

where in this chapter $\boldsymbol{A}$ and $\boldsymbol{B}$ are the *inverses* of the shape matrices of the two ellipsoids in the lab frame and $\boldsymbol{x}$ is the vector separating the centers of these ellipsoids. This expression apparently depends on λ in a complicated way, and the standard method for finding the contact parameter λ_c that minimizes $\mathcal{S}$ is to plug equation (3.2) into an optimization routine that does not require a gradient or Hessian (e.g., Brent's method[59]).

A brute force expansion of equation (3.2) shows that $\mathcal{S}(\lambda)$ can be written as a rational function. The term $\lambda(1 - \lambda)$ contributes a second-order polynomial to the numerator, while the inverse matrix contributes a second-order polynomial to the numerator and a third-order polynomial to the denominator. Thus,

$$\mathcal{S}(\lambda) = \frac{f(\lambda)}{g(\lambda)} = \frac{\sum_{i=1}^{4} f_i \lambda^i}{\sum_{i=0}^{3} g_i \lambda^i}, \tag{3.3}$$

where the f_i and g_i are functions of $\boldsymbol{A}$ and $\boldsymbol{B}$ and do not depend on λ. (In this chapter, λ^i means λ to the i-th power.)

This reformulation shows that maximizing the matrix quantity in equation (3.2) is equivalent to maximizing the rational function in equation (3.3). Because $\mathcal{S}(\lambda)$ is rational, the derivative $d\mathcal{S}/d\lambda = \mathcal{S}'(\lambda)$ is also rational. Maximizing $\mathcal{S}(\lambda)$ is therefore equivalent to finding the root of the numerator of $\mathcal{S}'(\lambda)$. Finding the root of a polynomial over the range $[0, 1]$ is, in some ways, an easier problem than maximizing the matrix quantity in equation (3.2).

Some simple calculus shows that the numerator of $\mathcal{S}'(\lambda)$ is a sixth-order polynomial. Let this polynomial be called $h(\lambda) = \sum_{i=0}^{6} h_i \lambda^i$, where the h_i are functions of the f_i and g_i. Because $h(\lambda)$ is just a polynomial, its analytical derivative is easy to calculate, and Newton's method is an efficient approach to find the root of $h(\lambda)$. The position of this root is the contact parameter λ_c. Once λ_c is found, it is a simple matter to compute $F = \mathcal{S}(\lambda_c)$.

When using Brent's method and the matrix formalism to find λ_c for the simulations described in this thesis, about 10 iterations were required to compute λ_c to within 10^{-6}. Computing the polynomial coefficients constitutes a higher overhead, but the cost of each iteration is lower. Newton's method also requires fewer steps, and in most cases less than 5 iterations were required to find the root of $h(\lambda)$. Altogether this improvement has led to a 1.5 times speedup for the computation of the entire PY potential for all but the smallest systems.

In this section, I will derive expressions for the coefficients f_i, g_i and h_i and demonstrate that the intermediate quantities used to compute the coefficients have certain properties that simplify the computation of the coefficients.

3.1.2 Coefficients of $\mathcal{S}$

The f_i and g_i depend on $\boldsymbol{A}$ and $\boldsymbol{B}$ in a complicated way. Writing expressions for these coefficients requires a careful consideration of the properties of $\boldsymbol{A}$ and $\boldsymbol{B}$, the cofactor matrices of $\boldsymbol{A}$ and $\boldsymbol{B}$, and another matrix $\widetilde{\boldsymbol{C}}$ that mixes these cofactor matrices. In this subsection, I will derive expressions for the entries of $\boldsymbol{A}$, $\boldsymbol{B}$, the cofactor matrices of $\boldsymbol{A}$ and $\boldsymbol{B}$, and $\widetilde{\boldsymbol{C}}$. Next I will define some auxiliary quantities A^*, B^*, and C^* using these matrices. The coefficients of $\mathcal{S}$ can be compactly written in terms of these auxiliary quantities.

Inverse shape matrices

Let the two shape matrices in their diagonal representations be $\boldsymbol{A}'$ and $\boldsymbol{B}'$. Let the rotation matrices be $\boldsymbol{R}$ and $\boldsymbol{S}$ such that the shape matrices in the lab frame are $\boldsymbol{R}\boldsymbol{A}'\boldsymbol{R}^T$

and $\boldsymbol{S}\boldsymbol{B}'\boldsymbol{S}^T$. Then the inverse shape matrix in the lab frame is

$$\boldsymbol{A} = \left(\boldsymbol{R}\boldsymbol{A}'\boldsymbol{R}^T\right)^{-1} \tag{3.4}$$

$$= \left(\boldsymbol{R}^T\right)^{-1}\boldsymbol{A}'^{-1}\boldsymbol{R}^{-1} \tag{3.5}$$

$$= \boldsymbol{R}\boldsymbol{A}'^{-1}\boldsymbol{R}^T \tag{3.6}$$

$$A_{ij} = \sum_m A'^{-1}_{mm} R_{im} R_{jm}. \tag{3.7}$$

Note that $\det \boldsymbol{A} = (\det \boldsymbol{A}')^{-1}$ and $\boldsymbol{A} = \boldsymbol{A}^T$. These results also hold for $\boldsymbol{B}$.

Cofactor matrices

The cofactor of the (i,j)-th entry of the matrix $\boldsymbol{A}$ is $(-1)^{i+j} M_{ij}$, where M_{ij} is the determinant of the submatrix obtained by removing the i-th row and j-th column from $\boldsymbol{A}$. The determinant of $\boldsymbol{A}$ can be written

$$\det \boldsymbol{A} = \sum_i A_{ij} M_{ij} \tag{3.8}$$

for any j, and the inverse of $\boldsymbol{A}$ is

$$\boldsymbol{A}^{-1} = \frac{\widetilde{\boldsymbol{A}}^T}{\det \boldsymbol{A}}, \tag{3.9}$$

where $\widetilde{\boldsymbol{A}}$ is the cofactor matrix for $\boldsymbol{A}$. The entries in the cofactor matrix are the cofactors of the corresponding entries of the original matrix. Because $\boldsymbol{A}$ is a 3×3 matrix, its cofactor matrix is easy to compute:

$$\widetilde{A}_{ij} = A_{i+1,j+1}A_{i+2,j+2} - A_{i+2,j+1}A_{i+1,j+2} \tag{3.10}$$

$$= \sum_{mn} A'^{-1}_{mm} A'^{-1}_{nn} \Big(R_{i+1,m} R_{j+1,m} R_{i+2,n} R_{j+2,n} \tag{3.11}$$

$$- R_{i+2,m} R_{j+1,m} R_{i+1,n} R_{j+2,n} \Big) \tag{3.12}$$

$$= \sum_m A'^{-1}_{m+1,m+1} A'^{-1}_{m+2,m+2} R_{im} R_{jm}, \tag{3.13}$$

where index addition is modulo 3 (e.g., $A_{i,3+1} \equiv A_{i,1}$) and I have used the fact that the rotation matrix $\boldsymbol{R}$ is equal to its own cofactor matrix. In this form, it is clear that $\widetilde{\boldsymbol{A}} = \widetilde{\boldsymbol{A}}^T$ and similarly $\widetilde{\boldsymbol{B}} = \widetilde{\boldsymbol{B}}^T$. These symmetries simplify the implementation of the algorithm.

Define also the matrix $\widetilde{\boldsymbol{C}}$ with entries

$$
\begin{aligned}
\widetilde{C}_{ij} = {} & (A_{i+1,j+1}B_{i+2,j+2} - A_{i+1,j+2}B_{i+2,j+1}) \\
& + (B_{i+1,j+1}A_{i+2,j+2} - B_{i+1,j+2}A_{i+2,j+1}) \,.
\end{aligned}
\tag{3.14}
$$

Note that the first bracketed term would be $\widetilde{A}_{ij}$ if the B's were replaced with A's, and that the second term is the same as the first but with the A's and B's reversed, so $\widetilde{\boldsymbol{C}}$ is a matrix that mixes the cofactor matrices of $\boldsymbol{A}$ and $\boldsymbol{B}$. Using the equations for A_{ij} and B_{ij}, one can find that

$$
\widetilde{C}_{ij} = \sum_{mn} A'^{-1}_{mm} B'^{-1}_{nn} \times (\text{four terms of form } RRSS) \,.
\tag{3.15}
$$

When written in this form it is straightforward to identify the terms that are symmetric under exchanges $i \leftrightarrow j$ and $m \leftrightarrow n$ and thereby show that $\widetilde{\boldsymbol{C}} = \widetilde{\boldsymbol{C}}^T$.

Because $\widetilde{\boldsymbol{A}}$ and $\widetilde{\boldsymbol{B}}$ are functions of the parameters of a single ellipsoid, those matrices can be computed once per ellipsoid at the beginning of an analysis of a given configuration of ellipsoids. The matrix $\widetilde{\boldsymbol{C}}$ depends on $\boldsymbol{A}$ and $\boldsymbol{B}$ together, so $\widetilde{\boldsymbol{C}}$ must be computed for every pair of ellipsoids.

Expressions for f_i and g_i

Define also

$$
A^* = \boldsymbol{x}^T \widetilde{\boldsymbol{A}} \boldsymbol{x} = \sum_{ij} x_i x_j \widetilde{A}_{ij}
\tag{3.16}
$$

and similarly define B^* and C^*. By brute force expansion of $\mathcal{S}$ in equation (2.9), it can be shown that the numerator of $\mathcal{S}$ has coefficients

$$
f_1 = A^*
\tag{3.17}
$$
$$
f_2 = -3A^* + C^*
\tag{3.18}
$$
$$
f_3 = 3A^* + B^* - 2C^*
\tag{3.19}
$$
$$
f_4 = -A^* - B^* + C^*.
\tag{3.20}
$$

For the denominator define

$$
D^* = \sum_{ij} A_{ij} \widetilde{B}_{ij}
\tag{3.21}
$$

$$
E^* = \sum_{ij} B_{ij} \widetilde{A}_{ij}.
\tag{3.22}
$$

16

(D^* is called the Frobenius inner product of A and $\widetilde{B}$.) The coefficients of the denominator of $\mathcal{S}$ are then

$$g_0 = \det \boldsymbol{A} \tag{3.23}$$

$$g_1 = -3 \det \boldsymbol{A} + E^* \tag{3.24}$$

$$g_2 = 3 \det \boldsymbol{A} + D^* - 2E^* \tag{3.25}$$

$$g_3 = -\det \boldsymbol{A} + \det \boldsymbol{B} - D^* + E^*. \tag{3.26}$$

3.1.3   Coefficients of $\mathcal{S}'$

Straightforward differentiation of the rational expression for $\mathcal{S}$ shows that the numerator of $\mathcal{S}'$ has coefficients

$$h_0 = f_1 g_0 \tag{3.27}$$

$$h_1 = 2f_2 g_0 \tag{3.28}$$

$$h_2 = 3f_3 g_0 + f_2 g_1 - f_1 g_2 \tag{3.29}$$

$$h_3 = 4f_4 g_0 + 2f_3 g_1 - 2f_1 g_3 \tag{3.30}$$

$$h_4 = 3f_4 g_1 + f_3 g_2 - f_2 g_3 \tag{3.31}$$

$$h_5 = 2f_4 g_2 \tag{3.32}$$

$$h_6 = f_4 g_3. \tag{3.33}$$

The derivative of $h(\lambda) = \sum_{i=0}^{6} h_i \lambda^i$ is simply $h'(\lambda) = \sum_{j=1}^{6} j h_j \lambda^{j-1}$. Applying Newton's method to find the root of h' is straightforward. However, Newton's method often moves outside the range $[0, 1]$ in which the root λ_c must lie. In my implementations, I substitute a bisection step when Newton's method attempts to move to a position outside the range of possible solutions.

3.1.4   Special case: $\boldsymbol{A}' = \boldsymbol{B}'$ with two equal eigenvalues

If $\boldsymbol{A}' = \boldsymbol{B}'$ and two of the diagonal elements of $\boldsymbol{A}'$ are equal, then the term g_3 vanishes. This special case arises frequently, since the ellipsoids used in simulations are often ellipsoids of revolution, which have two equal semiaxes. Furthermore, once g_3 vanishes, then h_6 vanishes, so the root-finding algorithm needs to compute a fifth- rather than a sixth-order polynomial in this case. The proof that g_3 vanishes under these circumstances is laborious but not complex.

If $\boldsymbol{A}' = \boldsymbol{B}'$, then $\det \boldsymbol{A} = \det \boldsymbol{B}$, so the first two terms of g_3 cancel, leaving $-D^* + E^*$.

To show that $D^* = E^*$, rewrite D^* as

$$D^* = \sum_{ij} \left(\sum_m A'^{-1}_{mm} R_{im} R_{jm} \right) \left(\sum_n B'^{-1}_{n+1,n+1} B'^{-1}_{n+2,n+2} S_{in} S_{jn} \right) \tag{3.34}$$

$$= \sum_{mn} A'^{-1}_{mm} B'^{-1}_{n+1,n+1} B'^{-1}_{n+2,n+2} \left(\sum_i R_{im} S_{in} \right) \left(\sum_j R_{jm} S_{jn} \right) \tag{3.35}$$

$$= \sum_{mn} A'^{-1}_{mm} B'^{-1}_{n+1,n+1} B'^{-1}_{n+2,n+2} \left[\left(\boldsymbol{R}^T \boldsymbol{S} \right)_{mn} \right]^2. \tag{3.36}$$

Similarly,

$$E^* = \sum_{mn} B'^{-1}_{mm} A'^{-1}_{n+1,n+1} A'^{-1}_{n+2,n+2} \left[\left(\boldsymbol{S}^T \boldsymbol{R} \right)_{mn} \right]^2 \tag{3.37}$$

$$= \sum_{mn} B'^{-1}_{mm} A'^{-1}_{n+1,n+1} A'^{-1}_{n+2,n+2} \left[\left(\boldsymbol{R}^T \boldsymbol{S} \right)_{nm} \right]^2. \tag{3.38}$$

Since $\boldsymbol{A}' = \boldsymbol{B}'$, the only difference between D^* and E^* is the order of the subscripts in the last term.

Now because two eigenvalues of $\boldsymbol{A}$ and $\boldsymbol{B}$ are equal, set (without loss of generality) $A'_{11} = A'_{22}$. Then D^* and E^* consist of three groups of terms: ones proportional to $\left(A'^{-1}_{11} \right)^3$, to $\left(A'^{-1}_{11} \right)^2 A'^{-1}_{33}$, and to $A'^{-1}_{11} \left(A'^{-1}_{33} \right)^2$. These groups occur for mn: $13, 23$; $11, 22, 33, 12, 21$; and $31, 32$ respectively. Swapping $m \leftrightarrow n$ swaps the first and last group of $\boldsymbol{A}'$ and $\boldsymbol{B}'$ but leaves the middle group unchanged. Thus, swapping $m \leftrightarrow n$ in the sum requires that the indices on the $\boldsymbol{A}'$ and $\boldsymbol{B}'$ also be swapped, bringing them back to their original places. Thus, each term in the D^* and E^* sums are equal, so $D^* = E^*$ and $g_3 = 0$.

3.2 Cutoffs for the PY potential

Because the PY potential is both position- and orientation-dependent, it is inappropriate to cut off the potential using the intercenter distance alone. This formulation can produce discontinuities in a simulation using periodic boundary conditions, since there are situations in which one image of an interacting ellipsoid has the minimum intercenter distance but not the minimum directional contact distance to the other interacting ellipsoid.

It is useful to rewrite the PY potential as $U = U_{\text{rep}} + U_{\text{att}}$, where

$$U_{\text{rep}} = 4\epsilon_0 G_{\text{rep}}^{-12} \tag{3.39}$$

$$U_{\text{att}} = -4\epsilon_0 G_{\text{att}}^{-6} \tag{3.40}$$

and $G_{\text{rep}} = \left[d_R^{(\text{rep})} + \sigma_0\right] \big/ \sigma_0$ as in equation (2.12). A potential with a Stoddard-Ford-like[60] cut off is then

$$U_{\text{rep}} = 4\epsilon_0 \left\{ G_{\text{rep}}^{-12} + G_c^{-12} \left[6 \left(\frac{G_{\text{rep}}}{G_c} \right)^2 - 7 \right] \right\}, \tag{3.41}$$

$$U_{\text{att}} = 4\epsilon_0 \left\{ -G_{\text{att}}^{-6} + G_c^{-6} \left[-3 \left(\frac{G_{\text{att}}}{G_c} \right)^2 + 4 \right] \right\}, \tag{3.42}$$

where G_c is the cut-off value for G. The gradients are

$$U_{\text{rep}}' = 48\epsilon_0 \left(-G_{\text{rep}}^{-13} G_{\text{rep}}' + G_c^{-14} G_{\text{rep}} G_{\text{rep}}' \right), \tag{3.43}$$

$$U_{\text{att}}' = 24\epsilon_0 \left(G_{\text{att}}^{-7} G_{\text{att}}' - G_c^{-8} G_{\text{att}} G_{\text{att}}' \right). \tag{3.44}$$

The derivatives of G can be computed from the derivatives of r_{AB} and F, which are known.[25,61] In this modified potential, G_{rep} and G_{att} reach zero smoothly at G_c.

It is usually more natural to define a cutoff distance d_c, and this can be easily converted to $G_c(d_c) = (d_c + \sigma_0)/\sigma_0$. When $G_{\text{rep}} = G_{\text{att}}$, the potential reaches a fraction α of its minimum value at a directional contact distance

$$\left(\alpha^{-1/6} - 1 \right) \sigma_0. \tag{3.45}$$

For example, $d_c \sim 1.2\sigma_0$ would cut off the potential at the surface where the absolute value of the potential had originally fallen to 1% of its minimum value.

3.3 General method for transforming site-site orientational gradients to rigid body gradients

3.3.1 Introduction

In coarse-grained modeling, it is common to construct rigid bodies from sites whose pair-wise interactions are known. Rigid bodies of LJ sites have been used to model ortho-terphenyl.[62] The Stockmayer particle, used in fluid models, consists of a LJ site and a dipole site.[63,64] Helix-forming 'dumbbell' building blocks are constructed from two LJ sites and a dipole.[65] Building blocks of PY ellipsoids and LJ sites have reproduced chiral clusters and capsid-like structures.[66,67] DNA can be modeled by a building block with one site for the backbone and one site for the base.[68]

More complex models might require multiple sites whose positions and orientations differ from those of the entire rigid body. In order to perform simulations using these

building blocks, it is necessary to transform the gradients of the potential with respect to the coordinates of the interacting sites into gradients with respect to the coordinates of the two rigid bodies. As will be reiterated here, transforming the translational gradients is trivial. Furthermore, in most cases, the orientational gradients can be transformed using properties specific to the potential. Here I provide a general method for transforming site-site orientational gradients to body-body gradients without any appeal to the form of the potential.

3.3.2 Definitions and notation

A rigid body I has a position $\boldsymbol{r}^I$ and angle-axis rotation $\boldsymbol{p}^I$. In the angle-axis framework, the orientation of the body I is described by $\boldsymbol{p}^I$: the body is transformed from some reference geometry to its lab frame orientation by rotating the body about the unit vector $\hat{\boldsymbol{p}}^I$ through an angle $|\boldsymbol{p}^I|$. Although $\boldsymbol{p}^I$ is sometimes called the angle-axis vector, $\boldsymbol{p}^I$ is not a vector in the proper sense, since simply adding the components of two angle-axis rotations is not equivalent to concatenating the two rotations they describe. Each $\boldsymbol{p}^I$ corresponds to a rotation matrix $\boldsymbol{R}^I$.

Body I consists of sites i, each with molecule frame position $\boldsymbol{r}^{i0}$, molecule frame angle-axis rotation $\boldsymbol{p}^{i0}$, and molecule frame rotation matrix $\boldsymbol{R}^{i0}$. Each site also has lab frame position $\boldsymbol{r}^i$, lab frame angle-axis rotation $\boldsymbol{p}^i$, and lab frame rotation matrix $\boldsymbol{R}^i$. Two rigid bodies I and J have a pairwise energy U^{IJ} that is the sum of the site-site energies U^{ij} over all sites i in body I and all sites j in body J.

In accordance with previous work,[61] $\boldsymbol{R}^I_\nu \equiv \partial \boldsymbol{R}^I / \partial p^I_\nu$. In accordance with typical usage, $R_{\alpha\beta}$ refers to the entry of the matrix $\boldsymbol{R}$ in row α and column β. The use of bold-face should make this use of notation unambiguous: $\boldsymbol{R}^I$ and $\boldsymbol{R}^I_\nu$ are both matrices, but $R^I_{\alpha\beta}$ is an entry of $\boldsymbol{R}^I$ and p^I_ν is a component of $\boldsymbol{p}^I$. I use the Einstein summation convention for matrix and vector indices. The metric is the identity in these cases, so upper and lower indices have no particular meaning.

3.3.3 Radial terms

The center-of-mass forces just add up, so

$$\frac{\partial U^{IJ}}{\partial \boldsymbol{r}^I} = \sum_{i \in I} \sum_{j \in J} \frac{\partial U^{ij}}{\partial \boldsymbol{r}^i}. \tag{3.46}$$

Since $U^{IJ} = U^{JI}$ and $U^{ij} = U^{ji}$, it follows that

$$\frac{\partial U^{IJ}}{\partial \boldsymbol{r}^J} = \sum_{i \in I} \sum_{j \in J} \frac{\partial U^{ij}}{\partial \boldsymbol{r}^j}. \tag{3.47}$$

In most cases where the potential U_{ij} does not depend on a bond angle, we can avoid computing the derivatives with respect to $\boldsymbol{r}^j$ because

$$\frac{\partial U_{ij}}{\partial \boldsymbol{r}^j} = -\frac{\partial U_{ij}}{\partial \boldsymbol{r}^i}. \tag{3.48}$$

3.3.4   Orientational terms

The orientational terms have contributions from both the site-site radial gradients and the site-site orientational gradients, since

$$\frac{\partial U^{IJ}}{\partial p_\nu^I} = \sum_{i \in I} \sum_{j \in J} \frac{\partial U^{ij}}{\partial p_\nu^I} \tag{3.49}$$

$$= \sum_{i \in I} \sum_{j \in J} \left(\frac{\partial \boldsymbol{r}^i}{\partial p_\nu^I} \frac{\partial U^{ij}}{\partial \boldsymbol{r}^i} + \frac{\partial \boldsymbol{p}^i}{\partial p_\nu^I} \frac{\partial U^{ij}}{\partial \boldsymbol{p}^i} \right). \tag{3.50}$$

The derivatives of U^{ij} are the site-site gradients that can be computed from each individual potential. This leaves the derivatives of the site coordinates $\boldsymbol{r}^i$ and $\boldsymbol{p}^i$ with respect to the body orientational coordinates $\boldsymbol{p}^I$.

Contributions from site-site radial terms

Previous work[61] has shown that

$$\boldsymbol{r}^i = \boldsymbol{r}^I + \boldsymbol{R}^I \boldsymbol{r}^{i0} \implies \frac{\partial \boldsymbol{r}^i}{\partial p_\nu^I} = \boldsymbol{R}_\nu^I \boldsymbol{r}^{i0}. \tag{3.51}$$

Methods for computing the rotation matrix derivative $\boldsymbol{R}_\nu^I$ are given in the same publication.

Contributions from site-site orientational terms

In the simplest case, the site and the molecule have the same orientation so that $\boldsymbol{p}^i = \boldsymbol{p}^I$, and $\partial \boldsymbol{p}^i / \partial \boldsymbol{p}^I$ in equation (3.50) is just the identity. However, if the site has some nonzero orientation $\boldsymbol{p}^{i0}$ in the molecule frame, then the derivative can be broken down by appealing

to the entries of the rotation matrices $\boldsymbol{R}^i$ that correspond to the relevant rotations $\boldsymbol{p}^i$:

$$\frac{\partial p_\mu^i}{\partial p_\nu^I} = \frac{\partial p_\mu^i}{\partial R_{\alpha\beta}^i} \frac{\partial R_{\alpha\beta}^i}{\partial p_\nu^I}. \tag{3.52}$$

The value of this approach is that it allows the second term $\partial \boldsymbol{R}^i/\partial \boldsymbol{p}^I$ to be written in terms of known values. The lab frame rotation matrix for site i is $\boldsymbol{R}^i = \boldsymbol{R}^I \boldsymbol{R}^{i0}$, where $\boldsymbol{R}^{i0}$, the molecule frame rotation matrix for site i, is constant. Thus,

$$\frac{\partial R_{\alpha\beta}^i}{\partial p_\nu^I} = \left(\boldsymbol{R}_\nu^I \boldsymbol{R}^{i0}\right)_{\alpha\beta}. \tag{3.53}$$

This matrix can be found by computing the matrix product of the rotation matrix derivative for the body, $\boldsymbol{R}_\nu^I$, and the body frame rotation matrix for the site, $\boldsymbol{R}^{i0}$. Note that the algorithm used to compute $\boldsymbol{R}_\nu^I$ from $\boldsymbol{R}^I$ may *not* be used to compute $\partial \boldsymbol{R}^i/\partial \boldsymbol{p}^I$ from $\boldsymbol{R}^i$. That approach would produce $\partial \boldsymbol{R}^i/\partial \boldsymbol{p}^i$, the derivatives of the lab frame rotation matrix for the site with respect to the lab frame angle-axis components for the site, which is of no help in working out equation (3.52).

The first term $\partial \boldsymbol{p}^i/\partial \boldsymbol{R}^i$ in equation (3.52) is more complicated. To compute the derivative of the site's angle-axis vector $\boldsymbol{p}^i$ with respect to the entries in the corresponding rotation matrix $\boldsymbol{R}^i$, we can appeal to the transformation from rotation matrices to angle-axis vectors:

$$\boldsymbol{p}(\boldsymbol{R}) = \frac{\arccos\left[\frac{1}{2}\left(\operatorname{Tr} \boldsymbol{R} - 1\right)\right]}{2\sqrt{1 - \frac{1}{4}\left(\operatorname{Tr} \boldsymbol{R} - 1\right)^2}} \begin{pmatrix} R_{32} - R_{23} \\ R_{13} - R_{31} \\ R_{21} - R_{12} \end{pmatrix} \tag{3.54}$$

$$\equiv X\boldsymbol{y}, \tag{3.55}$$

where $X \equiv \frac{1}{2}\arccos T/\sqrt{1 - T^2}$ and $T \equiv \frac{1}{2}(\operatorname{Tr} \boldsymbol{R} - 1)$. Noting that

$$\frac{\partial X}{\partial R_{\alpha\beta}} = \frac{1}{2\left(1 - T^2\right)}\left[T\frac{\arccos T}{2\sqrt{1 - T^2}} - \frac{1}{2}\right]\delta^{\alpha\beta} \tag{3.56}$$

$$\frac{\partial y_\gamma}{\partial R_{\alpha\beta}} = -\epsilon_\gamma{}^{\alpha\beta}, \tag{3.57}$$

where δ is the Kronecker delta and ϵ is the Levi-Civita symbol, we have one set of terms for the diagonal $\alpha = \beta$ and another set for the off-diagonals. Putting them together yields

$$\frac{\partial p_\mu^i}{\partial R_{\alpha\beta}^i} = \frac{1}{2\left(1 - T^2\right)}\left[T\frac{\arccos T}{2\sqrt{1 - T^2}} - \frac{1}{2}\right]\delta^{\alpha\beta}y_\mu - \frac{\arccos T}{2\sqrt{1 - T^2}}\epsilon_\mu{}^{\alpha\beta}, \tag{3.58}$$

where T and $\boldsymbol{y}$ are computed using $\boldsymbol{R}^i$.

It should be noted that the values $\partial p^i_\mu / \partial R^i_{\alpha\beta}$ are *not* the numerical reciprocals of $\partial R^i_{\alpha\beta} / \partial p^i_\mu = \left(\boldsymbol{R}^i_\mu\right)_{\alpha\beta}$. For most rotation matrices, all the elements of $\partial \boldsymbol{R} / \partial \boldsymbol{p}$ are nonzero, but $\partial \boldsymbol{p} / \partial \boldsymbol{R}$ will always have zero elements, since, e.g., $p_1(\boldsymbol{R})$ does not depend on R_{12}, R_{13}, R_{21}, or R_{31}. Analytically, it is clear that this approach is invalid since there is no one-to-one correspondence between rotations $\boldsymbol{p}$ and matrices $\boldsymbol{R}$ in this formalism. Angle-axis rotations and rotation matrices have a one-to-one relationship only if orthogonality of the matrices is enforced.

The values that make up $\partial \boldsymbol{p}^i / \partial \boldsymbol{R}^i$ need only be computed once per $\partial \boldsymbol{p}^i / \partial \boldsymbol{p}^I$. Combining the second term $\partial \boldsymbol{p}^i / \partial \boldsymbol{R}^i$ with $\partial \boldsymbol{R}^i / \partial \boldsymbol{p}^I$ in equation (3.52) requires a Frobenius (i.e., entry-wise matrix) product over α and β. This makes this method more computationally expensive than computing the body-body orientational gradients by appealing to the form of the specific potential where possible.

Chapter 4

Designing left-handed structures from right-handed building blocks

---

4.1   Introduction

Previous work[30,65,67] has shown that achiral building blocks modeled by sites interacting via an ellipsoidal Lennard-Jones-like potential self-assemble into chiral helical structures. This chirality was associated with broken symmetry in the minimum energy configuration of the dimer when two ellipsoids prefer to stack off-center rather than directly on top of one another.

If achiral building blocks can produce chiral structures, then what is the relationship between the chirality of building blocks and the chirality of the structures into which they assemble? It is natural to assume that molecular chirality unambiguously determines the chirality of a material so that a molecule of one particular handedness will produce materials of one particular handedness. Nevertheless, experimental evidence in amyloid fibrils,[69,70] insulin,[71,72] chiral phospholipids,[73] and cellulose[74] has demonstrated that this relationship is ambiguous: in nature, some right-handed molecules produce mixtures of right- and left-handed materials. It is unclear whether this ambiguity is due to properties of the building blocks, stochastic effects, or the specifics of the material's preparation.[75–78]

Probing the relationship between the chirality of building blocks and of their assembled structures requires a building block with adjustable chirality. Taking inspiration from experiments that produce helices of adjustable pitch using closely related molecular building blocks[79] and experiments that produce nematic phases with temperature-controlled pitch,[80,81] we have investigated the self-assembling structures that result from building blocks with adjustable chirality. These building blocks consisted of pairs of ellipsoids joined side-to-side in a rigid body that roughly resembles a bowtie. Over most of the
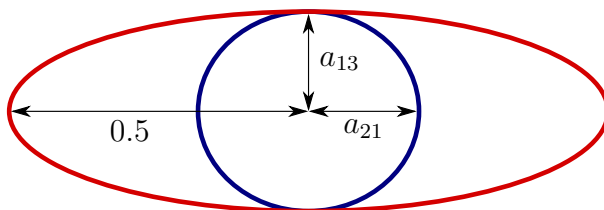
Figure 4.1: Cross-section of a Paramonov-Yaliraki[25] site as parameterized in this study, showing the repulsive ellipsoid (red), the attractive ellipsoid (blue), the repulsive equatorial semiaxis (0.5), the attractive equatorial semiaxis a_{21}, and the polar semiaxis a_{13} common to both ellipsoids. In these parameterizations, the two ellipsoids have a common equatorial plane and the same north and south poles.

parameter space we explored, right-handed bowties assemble into right-handed helices. However, certain sets of right-handed bowties assemble into left-handed helices. This behavior can be understood and predicted by analyzing the interaction of building blocks within a conformational subspace. Hence we provide quantitative design principles for constructing helical morphologies that only require experimental or simulation data within this subspace.

4.2   Methods

4.2.1   The Paramonov-Yaliraki potential

We used the Paramonov-Yaliraki (PY) potential[25] to model the interactions between the ellipsoids in the bowties. The individual PY sites are parametrized by the shapes of the repulsive and attractive ellipsoids, which are described by the three repulsive semiaxes, a_{1i}, and the three attractive semiaxes, a_{2i}. The parameterization used in this study is depicted in Figure 4.1. The repulsive and attractive ellipsoids are ellipsoids of revolution, and there are two free parameters: the polar semiaxis, a_{13}, which is common to both the repulsive and attractive ellipsoids, and the attractive equatorial semiaxis, a_{21}. Both a_{13} and a_{21} were systematically varied to elucidate design principles for the building blocks described below.

4.2.2   The building blocks

In this study we examined structures formed from identical rigid bodies composed of two equivalent PY sites (Figure 4.2). The centers of the sites were separated by the repulsive equatorial diameter, and the equatorial planes of the two sites in the building block intersected along a line that runs through the centers of both sites. The angle
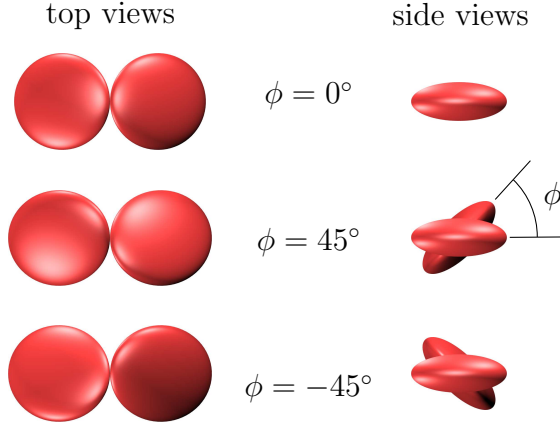
top views   side views

$\phi = 0°$

$\phi = 45°$

ϕ

$\phi = -45°$

Figure 4.2: The bowtie building block consists of two ellipsoids joined side-to-side. The dihedral angle ϕ is the angle between the equatorial planes of the two sites in the building block. The $\phi = 0°$ bowtie is achiral, the $\phi = 45°$ bowtie is right-handed, and the $\phi = -45°$ bowtie is left-handed. The side views show that the $\phi = \pm 45°$ bowties are mirror images of one another and cannot be superposed.

between the equatorial planes of the two sites is the dihedral angle ϕ.

For $\phi = 0°$, the two sites in the pair have the same orientation, and the equatorial planes of both sites coincide. In this case, the building block has D_{2h} symmetry and resembles a bowtie whose 'wings' are in perfect alignment. We considered building blocks with $\phi = 0°$ as limiting cases because the D_{2h} point group is achiral. Although building blocks with $\phi = 90°$ are also achiral, they do not form helices and we do not consider them here.

Bowties with $0° < \phi < 90°$ have D_2 symmetry and are therefore chiral. Bowties with dihedral angles $90° < \phi < 180°$ correspond to bowties with $-90° < \phi < 0°$ and are therefore mirror images of bowties with $0° < \phi < 90°$. As a convention, we define building blocks with $0° < \phi < 90°$ as right-handed. Holding a $\phi = 0°$ bowtie in front of you, a right-handed pair is then formed by twisting your right thumb through the angle ϕ away from your body while keeping your left hand fixed.

4.2.3 Exploring the landscape

Global potential energy minima for clusters of bowtie building blocks were identified using the basin-hopping[50,51,82] program GMIN,[53] which takes steps between local minima on the potential energy surface by randomly perturbing the position and orientation of each building block. Translational perturbations were uniformly distributed in a sphere with a radius of the same order as the building block's size (~ 2.0) and the orientational perturbations were uniformly distributed over ~ 1.0 radian. Perturbations that produced

overlap ($F < 1$) were discarded. If three sets of randomly-selected starting coordinates all produced the same lowest minimum, we accepted this structure as the putative global minimum. Otherwise we increased the number of basin-hopping steps until this criterion was met.

In studies of the structures formed by single PY sites, only a few hundred basin-hopping steps were required to reach consistency between runs starting from distinct configurations.[30] However, for the bowtie building blocks, tens of thousands of steps were required to reach the same kind of consistency. The increase in landscape complexity is probably due to the differences in the interaction range parameters σ_0 used in the two studies. The study of single-site PY building blocks used $\sigma_0 = 1$, 18, and 30, while in this study we used only $\sigma_0 = 1$. Decreasing the interaction length scales probably makes the energy landscape more rough[40,83,84] and makes it more difficult to identify global minima.

4.3 Results

4.3.1 Bowties assemble into helices

Over a large part of the parameter space of a_{13}, a_{21}, and ϕ, the global potential energy minimum for a cluster of these bowtie building blocks consists of segments of helices. Building blocks with $\phi = 0°$ assembled into achiral stacks, which are the limiting case of helices as the helix pitch diverges. We explored the region bounded by $0.1 \leq a_{13} \leq 0.5$ and $0.1 \leq a_{21} \leq 0.5$. Figure 4.3 shows a disconnectivity graph, a visualization of the energy landscape,[27,54] for one particular parameterization. As discussed in Section 2.5, most of the graph looks like a palm tree. There are, however, a few interesting features separate from the main funnel. In this example, the main funnel consists of minima that have two helical strands. In some, like minimum a, the two strands are joined. In others, like minimum b, 'caps' sit on top of or below the two strands. The bottom of the main funnel, minimum c, has two strands of equal length. The global minimum d, which is separated from the rest of the minima by a high barrier, is a single helix for this parameterization. Because the main funnel has a palm tree shape, we expect that a physical realization of these bowtie building blocks would self-assemble into helices or stacks.

Figure 4.4 shows the parts of this parameter space in which the global minimum energy configuration consists of stacks when the parameter ϕ is fixed at $0°$. The rotation angle Ω, which is the angle between corresponding axes of the bowties, quantifies the chirality of the helices. Stacks have $\Omega = 0°$. As a convention, we use $\Omega > 0°$ to describe a helix that is right-handed in the sense of Figure 4.5. In general, the chirality of the helix matches the chirality of the building block, so achiral building blocks ($\phi = 0°$) produce achiral stacks
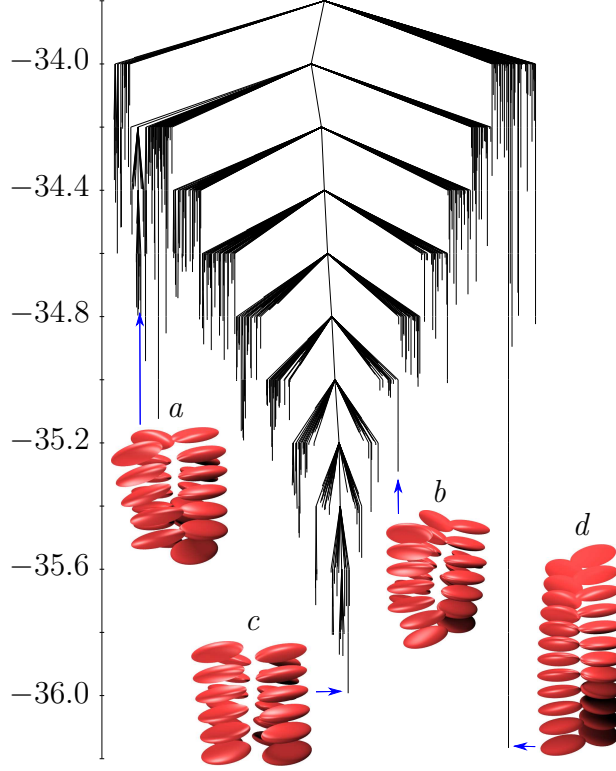
Figure 4.3: A part of the disconnectivity graph for 12 bowtie building blocks ($a_{13} = 0.15$, $a_{21} = 0.28$, $\phi = 23°$), showing the organization of the landscape for the minima at the bottom of the main funnel. Energies are measured in ϵ_0.

($\Omega = 0°$), right-handed building blocks ($\phi > 0°$) produce right-handed helices ($\Omega > 0°$), and left-handed building blocks ($\phi < 0°$) produce left-handed helices ($\Omega < 0°$).

4.3.2 Changes in morphology of the global minimum can be predicted

Because the global minima are generally helical in the region of parameter space we considered, it is useful to define a reduced potential energy landscape $U(\Omega, d)$ whose coordinates are the two parameters that describe a single helix: the distance d between the centers of adjacent bowtie building blocks and the rotation angle Ω. Because d is mostly unrelated to the investigation of chirality, the potential energy landscape can be further reduced to one with a single coordinate Ω by defining

$$\widetilde{U}(\Omega) = \min_d U(\Omega, d). \tag{4.1}$$

The function $\widetilde{U}$ is well-defined because U has only one minimum in d with Ω fixed.

The $\widetilde{U}$ landscape is useful for identifying morphological transitions in the parameter space. For example, $\widetilde{U}$ for bowties with $\phi = 0°$ and low attractive equatorial semiaxis a_{21}
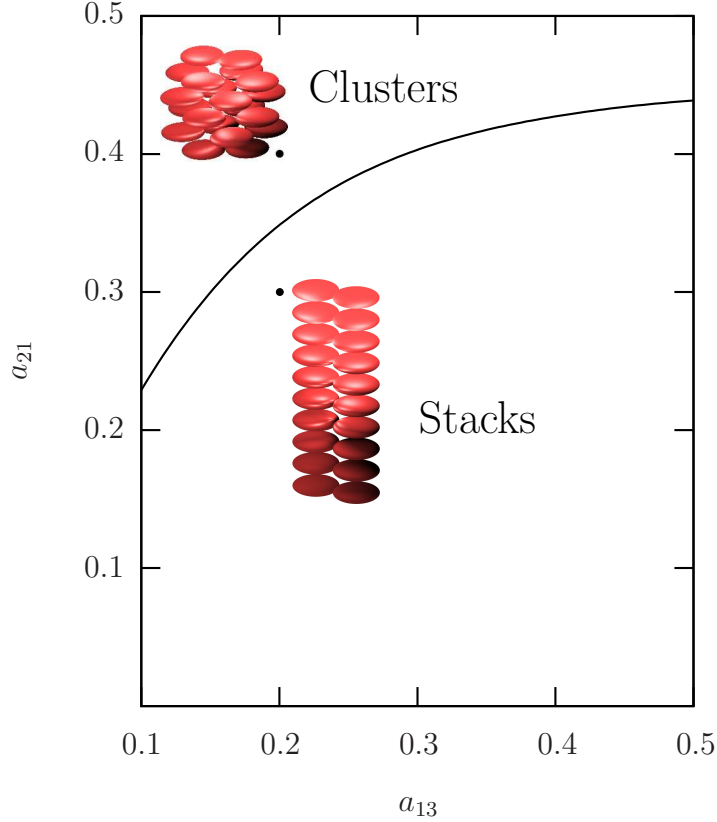
Figure 4.4: Regions of the parameter space of a_{13} and a_{21} for which the global minima of clusters composed of bowtie building blocks with $\phi = 0°$ consist of either stacks or more isotropic clusters of bowties. Two global minima for $N = 10$ and two parameterizations (black dots) are shown: one stack ($a_{13} = 0.2$, $a_{21} = 0.3$) and one cluster ($a_{13} = 0.2$, $a_{21} = 0.4$).

has one minimum at $\Omega = 0°$. For higher a_{21}, a local minimum of higher energy forms at $\Omega = 90°$. As a_{21} increases, the energy of the $\Omega = 90°$ minimum decreases and the energy of the $\Omega = 0°$ minimum increases. At a critical value of a_{21}, the two minima are equal in energy. At this point in the parameter space, the $\Omega = 0°$ minimum is no longer the global minimum as viewed in the reduced energy landscape with coordinates d and Ω. It is also at precisely this value of a_{21} that the configuration corresponding to the minimum in $\widetilde{U}$ is no longer a local minimum in the complete $6N$-dimensional landscape, where N is the number of building blocks. Hence this value of a_{21} represents the boundary of the helix-forming part of the parameter space for $\phi = 0°$ shown in Figure 4.4. A similar analysis applies for $\phi \neq 0°$, but here the minima in $\widetilde{U}$ are displaced away from $\Omega = 0°$ due to the broken symmetry.

In general, increasing a_{21} out of the helix-producing region of the parameter space yields structures that are more and more isotropic. At first, the helix breaks into a

'ladder' where adjacent bowties are staggered. For higher values, the helix bends over and loses its helical topology. For very high values of a_{21}, the potential energy minima are clusters with no particular directionality (Figure 4.4).

4.3.3   Using single helices

For a small number of building blocks ($N \lesssim 10$), the global minimum energy configuration consists of a single helix. For larger N, the global minimum consists of multiple helices attached side by side. Although it is more energetically favorable for bowties to stack on top of one another than to attach side by side, forming multiple helices breaks a single top-to-bottom contact and creates multiple side-to-side contacts. Hence this change in structure is energetically favorable for larger N. The configuration of the global minimum also depends on a_{13}, a_{21} and ϕ. For example, in Figure 4.3, the single strand is the global minimum. In the system with the same N, a_{13}, and a_{21} but with ϕ changed from 23° to 0°, the global minimum is not a single stack analogous to the single helix in Figure 4.3. Instead, the global minimum consists of two associated stacks analogous to those at the bottom of the main funnel in Figure 4.3. In general, the global minimum is not a single helix.

Having verified that the global potential energy minimum configurations all consist of helices or achiral stacks, we measured the relationship between the dihedral angle ϕ of the building blocks and the rotation angle Ω of single helices. Although a single helix is usually not the global minimum, the relationship between ϕ and Ω is much clearer in this minimum, since the interactions between side-by-side strands cause the rotation angle of the global minima to depend strongly on N. To measure $\Omega(\phi)$ without this complication, we set up long ($N = 100$) helices of bowtie building blocks with $0.1 < d < 1.0$ and $-90° < \Omega < 90°$ and evaluated their energies without relaxing the structure. We then relaxed the helix with the lowest energy. The result was always a single helix, that is, the single minimum on the $\widetilde{U}$ landscape for $N = 100$.

Because the helices were so long, edge effects were negligible: the rotation angles between the middle ten building blocks were equal to one another to within less than 0.001°, and these angles changed by less than 1% when the number of building blocks in the helix was changed to either $N = 50$ or $N = 200$. Hence the rotation angle between the two centermost building blocks in a single $N = 100$ stack provided a reasonable measure of Ω for a given ϕ. Although the precise numerical relation between ϕ and Ω in the global minima is different from the relation in the single helices we measured, the general trends described below appear to apply in both cases.
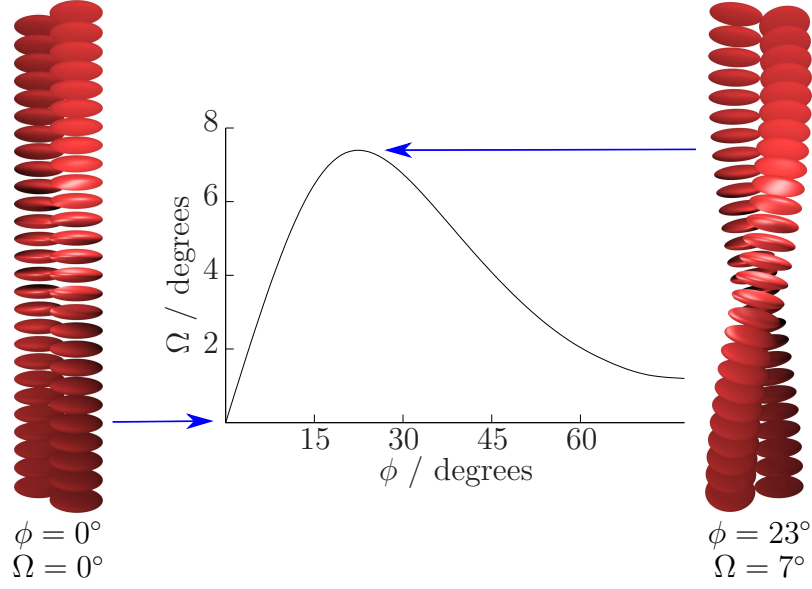
Figure 4.5: The relation $\Omega(\phi)$ for bowtie building blocks composed of PY sites of intermediate anisotropy ($a_{13} = 0.15$, $a_{21} = 0.28$). The helices are segments of the $N = 100$ helices used to compute the relationship $\Omega(\phi)$ shown in the graph. The curve in the graph terminates at the critical value of ϕ after which the local minimum energy configuration is no longer a helix.

4.3.4 The chirality of the building block determines the chirality of the helix

The relationship between the building block dihedral angle ϕ and the helix rotation angle Ω exhibits two distinct characteristics across the helix-forming parameterizations of a_{13} and a_{21}: Ω is mostly proportional to ϕ when ϕ is small, and Ω falls with increasing ϕ when ϕ is beyond the linear regime. For example, Figure 4.5 shows $\Omega(\phi)$ for a bowtie composed of ellipsoids of intermediate anisotropy. Achiral building blocks ($\phi = 0°$) produce an achiral stack ($\Omega = 0°$). For $\phi \lesssim 15°$, Ω is proportional to ϕ, and Ω falls for $\phi \gtrsim 20°$.

The linear relation is caused by *in-chain attraction* and the competing trend is caused by *cross-chain repulsion*. The relative importance of these two effects can be tuned via the parameters a_{13} and a_{21}.

4.3.5 In-chain attraction causes Ω to increase linearly with ϕ

Attraction between corresponding attractive ellipsoids of nearest-neighbor building blocks leads to the linear relationship between ϕ and Ω. In stacks with small ϕ, the value of Ω is the one that minimizes the distance between the north pole of the lower ellipsoid and the south pole of the upper ellipsoid. If the distance between the centers of the bowties

were fixed at d, the distance between the two poles would be

$$
\left\{ \left[a_{21}(1 - \cos\Omega) - a_{13}\sin\frac{\phi}{2}\sin\Omega \right]^2 \right.
$$
$$
\left. + \left[-a_{21}\sin\Omega + a_{13}\sin\frac{\phi}{2}(1 + \cos\Omega) \right]^2 + \left[2a_{13}\cos\frac{\phi}{2} - d \right]^2 \right\}^{1/2}, \quad (4.2)
$$

which is minimized when

$$
\Omega^* = \arctan\left[\frac{2\,(a_{13}/a_{21})\sin(\phi/2)}{1 - (a_{13}/a_{21})^2\sin^2(\phi/2)} \right]. \quad (4.3)
$$

For $a_{13} \ll a_{21}$, $\Omega^* \approx 2\,(a_{13}/a_{21})\sin(\phi/2)$. Since $2\sin(\phi/2) \approx \phi$ to within 5% for $0° < \phi < 60°$, we see that $\Omega^* \approx (a_{13}/a_{21})\,\phi$. This analysis quantitatively predicts the slope of the linear parts of the $\Omega(\phi)$ curves.

Decreasing the attractive equatorial semiaxis a_{21} increases the range of ϕ over which Ω is linear. In the limit $a_{21} \to 0$, the attractive ellipsoids reduce to rods whose endpoints lie at the poles of the two ellipsoids. The point of closest approach between the attractive ellipsoids in a chain will be at the ends of rods. In this case, it is clear that in-chain attraction seeks to minimize the distance between the poles of the two ellipsoids.

The energy of the helices increases as ϕ increases until some maximum value of ϕ. This critical value decreases from about 60° for larger a_{21} down to 0° as a_{21} reaches the boundary where the morphology of the global minimum changes for $\phi = 0°$ (Figure 4.4). Increasing ϕ beyond this value causes the helix to collapse into a more isotropic cluster. The increased energy and consequently decreasing stability are due to the increasing distance of closest approach between attractive ellipsoids in the same chain.

4.3.6   Cross-chain repulsion causes Ω to fall with ϕ

The decrease in Ω at larger ϕ is easy to understand by considering the $\widetilde{U}$ landscape. The minimum energy structures in $6N$-dimensional space correspond to minima on this surface, so the gradients of the four energy contributions (in-/cross-chain and attractive/repulsive) with respect to Ω at the minimum determine the relative importance of the various effects. At these minima, in-chain attraction biases Ω to higher values, but cross-chain repulsion causes Ω to fall to the observed smaller values. Thus, cross-chain repulsion dominates the behavior of Ω for larger ϕ.

Because the points of closest approach for the repulsive ellipsoids are at the 'tips' of the bowtie's 'wings', nearly isotropic repulsive ellipsoids have a cross-chain repulsion that remains mostly constant with ϕ (Figure 4.6a). In this case, the behavior of Ω is wholly
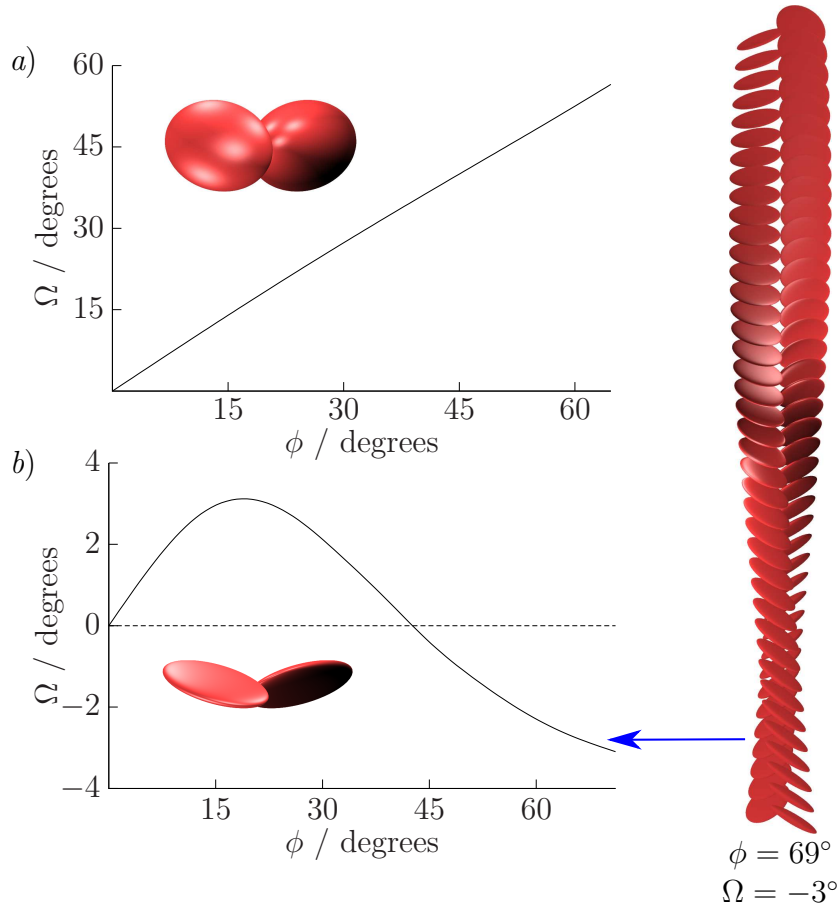
Figure 4.6: *a)* A right-handed bowtie building block composed of nearly isotropic PY sites ($a_{13} = 0.41$, $a_{21} = 0.1$) and the corresponding relation $\Omega(\phi)$. *b)* A right-handed bowtie building block composed of highly anisotropic PY sites ($a_{13} = 0.1$, $a_{21} = 0.23$) and the corresponding relation $\Omega(\phi)$. The building blocks are right-handed for all values of ϕ shown, but the resulting structures are right-handed for $0° < \phi \lesssim 42°$ and left-handed for $\phi \gtrsim 42°$, as in the left-handed helix shown.

dominated by the in-chain attraction. Conversely, highly anisotropic ellipsoids accentuate the effects of cross-chain repulsion. In fact, PY sites with disk-like ellipsoids have cross-chain repulsion that can *reverse* the handedness of the resulting helix (Figure 4.6*b*). In these cases, an achiral building block ($\phi = 0°$) produces an ahelical structure ($\Omega = 0°$); a right-handed building block ($\phi \approx 20°$) produces a right-handed structure ($\Omega > 0°$); but a different right-handed building block *of the same family of structures* ($\phi \approx 60°$) produces a *left-handed* structure ($\Omega < 0°$). Because Ω varies smoothly with ϕ, there is also a right-handed building block ($\phi \approx 43°$) that produces an achiral structure ($\Omega = 0°$).

33

4.3.7 Geometrical trends

The spacing between the bowties along the axis of the helix depends nearly linearly on the polar semiaxis a_{13} according to $d \approx 2.3\,a_{13}$ when ϕ is small. The value of the attractive equatorial semiaxis a_{21} has little effect on d, since the organization of the helix along its axis is due mostly to the polar axes rather than the equatorial axes. Values of d differ significantly from the small ϕ limit when cross-chain repulsion begins to influence Ω, since then the organization along the axis is affected by the interaction of the 'wings' of the bowties, whose position depends on ϕ. Because d is mostly insensitive to ϕ, the helix pitch, which is proportional to d/Ω, scales like ϕ^{-1} for small ϕ.

4.4 Conclusions

It is important to note we did not explicitly encode the model for the bowtie building blocks so that right-handed building blocks would produce assemblies of both chiralities. Instead, this behavior emerged from a simple building block and the anisotropy inherent in the PY sites. To the best of our knowledge, this bowtie building block is the first model that produces both right- and left-handed structures from right-handed building blocks.

Designing building blocks that assemble into fiber-like superstructures is an important theme in supramolecular chemistry.[85] As noted in previous research on families of single molecules that assemble into helical superstructures of varying chirality,[79] nanostructures whose structural angles could be adjusted dynamically might have applications in selective stereochemistry and nonlinear optics.

Chapter 5

Rigid bodies with PY sites: further designs

5.1   Bowties with long range interactions

The two-site rigid bodies discussed in Chapter 4 interacted via a short-range potential ($\sigma_0 = 1$). Although short-range potentials are easier to interpret as analogues of short-range forces between nanostructures, using larger σ_0 permits different parameterizations of the PY sites from Chapter 4. Consider the parameterization in Figure 5.1. Because the equatorial semiaxes of the repulsive and attractive ellipsoids are equal, there is an excluded-volume-type interaction in the equatorial plane. However, in this parameterization the attractive polar semiaxis is greater than the repulsive polar semiaxis. In a simulation with $\sigma_0 = 1$, the ellipsoids would stack on top of one another and interpenetrate. Though there is nothing wrong with overlapping configurations, they do create a very rough landscape whose low-lying minima are difficult to find. This propensity for overlap can be overcome by increasing the interaction length σ_0, which smooths the landscape (Sections 2.2.3 and 4.2.3).

For example, a system of six particles with these parameters and $\sigma_0 = 12$ assembles into a single helix for small dihedral angles ϕ (Figure 5.2). In light of previous research,[30] it is not surprising that the helix's rotation angle Ω is nonzero even when $\phi = 0°$. Just as with the $\sigma_0 = 1$ bowties discussed in Chapter 4, the helices break into a ladder morphology when ϕ is increased beyond some critical value (Figure 5.2c). Increasing ϕ further causes the ladders to collapse into two-dimensional clusters in which the centers of the bowties all lie in a plane (Figure 5.2d).

Increasing the number of particles in the system requires increasing σ_0 in order to prevent overlap. For a system of 100 particles, $\sigma_0 = 40$ was sufficient to prevent bowties with the same parameters from overlapping. In this system, the low-lying minima for small ϕ consist of multiple helices of bowties wrapping around a common center that has
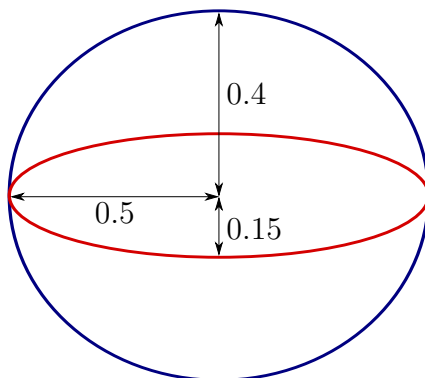
Figure 5.1: Cross-section of a Paramonov-Yaliraki[25] site used to make up the bowtie rigid bodies in simulations with $\sigma_0 > 1$. The repulsive ellipsoid of revolution (red) is contained inside the attractive ellipsoid of revolution (blue).

some smaller helices inside (Figure 5.3). As ϕ increases, these low-lying minima become less prolate. Between $\phi = 0°$ and $\phi = 46°$, the ratio of the two larger principal moments of inertia to the smaller one decreased from about 1.4 to about 1.2. The structure shown for $\phi = 90°$ is actually oblate: there are two small principal moments of inertia and one large one.

Parametrizations like the one shown in Figure 5.1 present a problem because the value of σ_0 needed to produce interesting results depends on N.

5.2 Four-site rigid bodies

Rigid bodies of PY sites should be sufficient for modeling molecules with four-fold symmetry. The chiral disk-shaped molecule synthesized and characterized by Engelkamp, Middelbeek, and Nolte[86] has four benzo crown ether moieties attached to a phthalocyanine ring. The structure of the molecule and the four-site rigid body inspired by it are shown in Figure 5.4. Characterization of the molecule showed that it self-assembles into fibers consisting of right-handed helices wound around one another in a left-handed superstructure.

This complementarity of handednesses is essential for good packing of the building blocks. The helices assembled from these four-site building blocks have ridges corresponding to the four corners and grooves corresponding to the grooves between the PY ellipsoids. For structures to maximize the number of contacts between constituent building blocks, the ridge of one helix must fit into the groove of its neighbor. Equilibrium structures of the four-site building block that reproduce one configuration with this type of complementarity are shown in Figure 5.5.
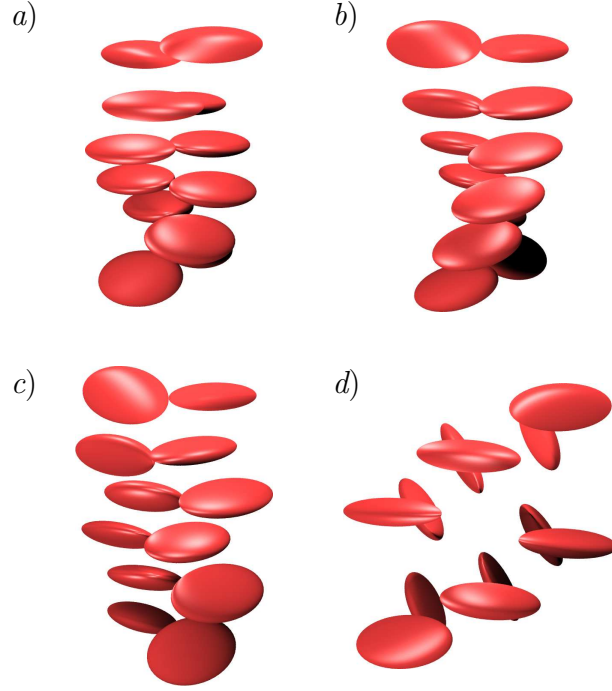
Figure 5.2: Global minima for six bowtie building blocks with $\sigma_0 = 12$ and the parameters shown in Figure 5.1. Only the repulsive ellipsoids are shown. *a)* $\phi = 0°$ *b)* $\phi = 23°$ *c)* $\phi = 34°$ *d)* $\phi = 57°$
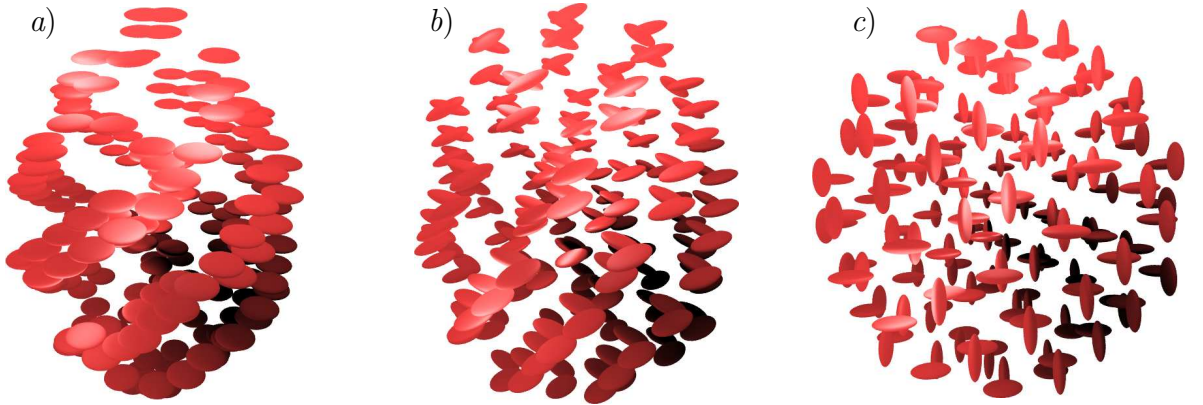
Figure 5.3: Low-lying minima for 100 bowtie building blocks with $\sigma_0 = 40$ and the parameters shown in Figure 5.1. *a)* $\phi = 0°$. The up-down axis is the principal axis with the small moment of inertia. *b)* $\phi = 46°$, with the same orientation. *c)* $\phi = 90°$. The axis perpendicular to the page is the principal axis with the large moment of inertia; this is a top-down view of the cluster.
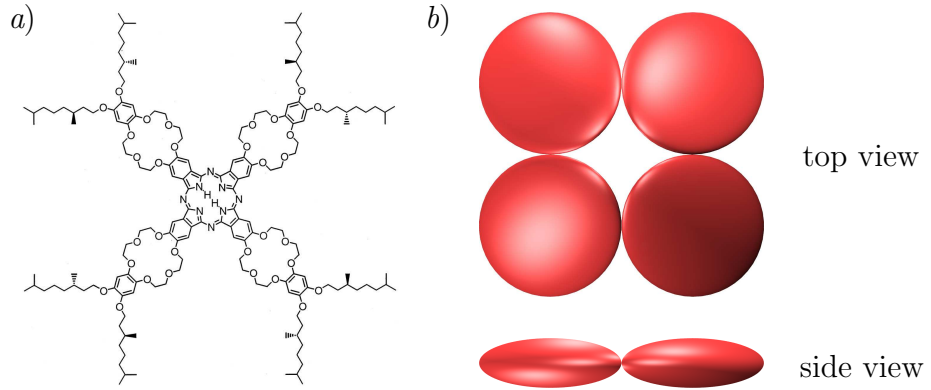
Figure 5.4: *a)* A chiral disk-shaped molecule.[86] *b)* An achiral rigid body constructed from four PY sites. The major semiaxes of all four ellipsoids lie in a plane, and their centers are separated by twice the length of the repulsive major semiaxes.
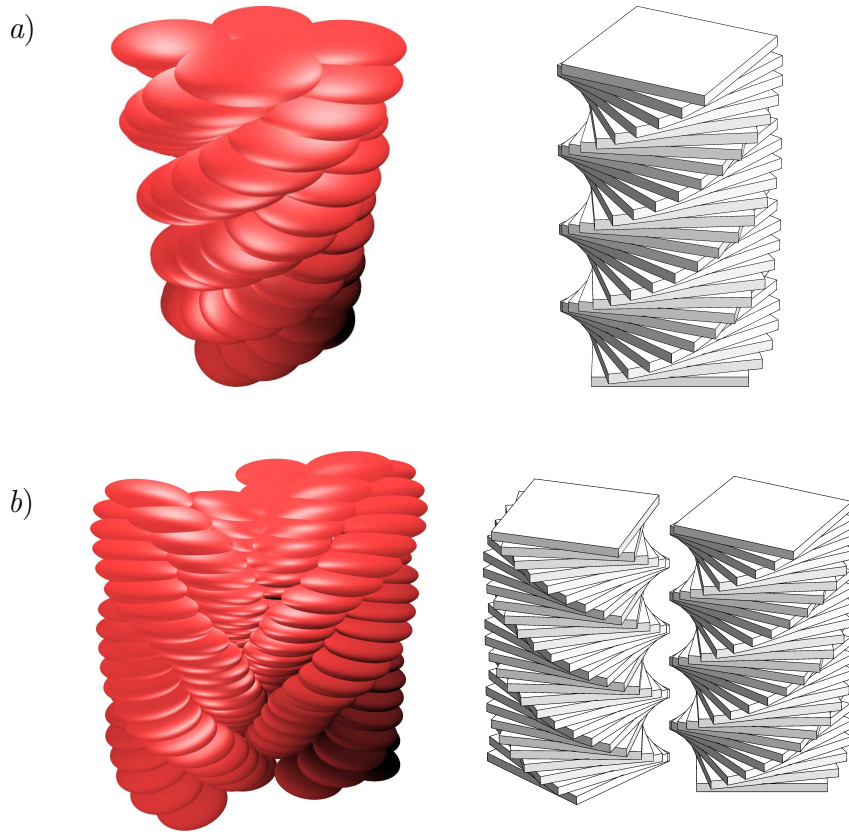
Figure 5.5: Equilibrium structures of four-site building blocks ($a_{11} = a_{12} = 0.5$, $a_{13} = 0.175$, $a_{21} = a_{22} = 0.55$, $a_{23} = 0.265$, $\sigma_0 = 1$) and schematics of the structures. *a)* A single twisting stack. *b)* Two twisting stacks of opposite handedness whose grooves and ridges are complementary.

Chapter 6

Chiral polar potential

6.1 Chiral interactions without chiral structures

In Chapter 4, chirality was introduced by constructing chiral bowtie building blocks. Each individual ellipsoid in the building block was achiral, and the interactions between individual ellipsoids were achiral, as neither the ECF nor the PY potential has any inherent preference for one handedness or the other. The interaction between whole building blocks, however, was chiral and produced chiral assemblies.

A coarse-grained chiral potential can reproduce the chiral interactions between building blocks without any reference to a particular building block structure. If a single chiral site can reproduce the effects of multiple achiral sites, the simulation might be less computationally expensive. This simplification also clarifies the behavior of the potential by removing the intermediate step in which the structure of the building block determines the chirality of the interaction between building blocks. Instead, the chirality of the interaction must be explicitly encoded in the potential. In this chapter, I present a coarse-grained single-site chiral potential and, as a proof of concept, use it to reproduce the structures exhibited by systems of chiral rod-like viruses.

6.2 The potential

The potential

$$U = -\frac{\mu^2 \sigma^3}{r^3} \left[\cos\alpha \left(\hat{\boldsymbol{\mu}}^i \cdot \hat{\boldsymbol{\mu}}^j \right) + \sin\alpha \left(\hat{\boldsymbol{\mu}}^i \times \hat{\boldsymbol{\mu}}^j \right) \cdot \hat{\boldsymbol{r}} \right] \tag{6.1}$$

describes the pairwise interaction between two chiral poles $\boldsymbol{\mu}^i$ and $\boldsymbol{\mu}^j$, where $|\boldsymbol{\mu}^i| = |\boldsymbol{\mu}^j| = \mu$, separated by $\boldsymbol{r}$. The length scale of the interaction is provided by σ. The angle α specifies the chirality of the interaction. The gradients of this potential are provided in
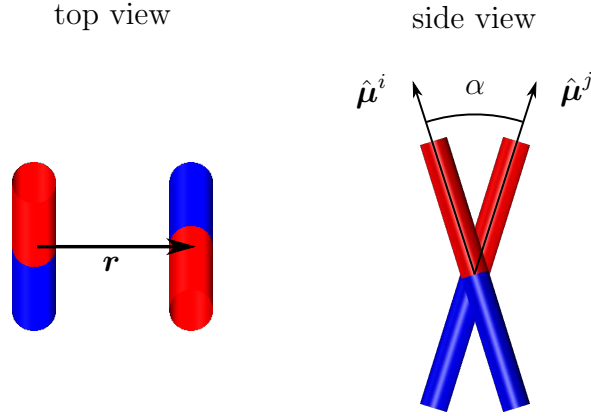
Figure 6.1: The minimum energy configuration for a dimer of chiral poles $\hat{\boldsymbol{\mu}}^i$ and $\hat{\boldsymbol{\mu}}^j$ parametrized by the angle α when the intercenter distance is fixed.

Section A.1.

The $\hat{\boldsymbol{\mu}}^i \cdot \hat{\boldsymbol{\mu}}^j$ term is similar to the first term in the potential for a dipole. This term favors orientations in which $\hat{\boldsymbol{\mu}}^i$ and $\hat{\boldsymbol{\mu}}^j$ are parallel, since U has an overall minus sign. The $\left(\hat{\boldsymbol{\mu}}^i \times \hat{\boldsymbol{\mu}}^j\right) \cdot \hat{\boldsymbol{r}}$ term, on the other hand, favors orientations in which $\hat{\boldsymbol{\mu}}^i$ and $\hat{\boldsymbol{\mu}}^j$ are at right angles and $\hat{\boldsymbol{\mu}}^i \times \hat{\boldsymbol{\mu}}^j$ is parallel to $\hat{\boldsymbol{r}}$. If the distance r is fixed, the dimer's minimum energy configuration has the two chiral poles oriented such that $\hat{\boldsymbol{\mu}}^i \times \hat{\boldsymbol{\mu}}^j$ is parallel to $\hat{\boldsymbol{r}}$ (Figure 6.1). In this case, $\hat{\boldsymbol{\mu}}^i \cdot \hat{\boldsymbol{\mu}}^j = \cos\theta$ and $\left(\hat{\boldsymbol{\mu}}^i \times \hat{\boldsymbol{\mu}}^j\right) \cdot \hat{\boldsymbol{r}} = \sin\theta$, where θ is the angle separating the poles. The potential is then proportional to

$$\cos\alpha\cos\theta + \sin\alpha\sin\theta = \cos(\alpha - \theta), \tag{6.2}$$

so the angle θ separating the chiral poles in the minimum energy configuration is α when $0 < \alpha < \pi$.

For $\alpha = 0$, the interaction is achiral, and the poles prefer to be aligned. For $\alpha = \pi$, the interaction is still achiral, but the poles prefer to be antiparallel. For $\alpha = \pi/2$, the interaction is achiral if the two ends of the pole are indistinguishable. For $-\pi < \alpha < 0$, the dimer's minimum energy configuration has the two chiral poles separated by an angle $|\alpha|$ such that $\hat{\boldsymbol{\mu}}^i \times \hat{\boldsymbol{\mu}}^j$ is *anti*parallel to $\hat{\boldsymbol{r}}$. Thus, reversing the sign of α reverses the chirality of the interaction.

Because $U \propto r^{-3}$, this potential must be combined with a repulsive core to prevent a singularity at $r = 0$.
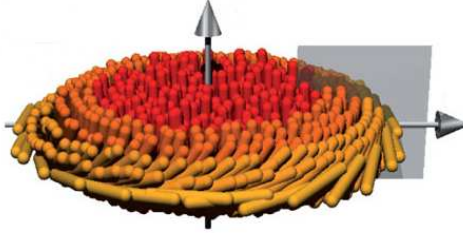
Figure 6.2: Illustration of an *fd* virus membrane observed in experiment (reproduced from Gibaud et al.[24]).

6.3 Application to modeling of systems of chiral rod-like viruses

The *fd* bacteriophage has been used as a model system for comparing theoretical systems of rod-like particles with experiment.[87] An *fd* virus consists of about 2700 copies of a coat protein wrapped around a single loop of DNA. It is 880 nm long and has a diameter of 6.6 nm, yielding an aspect ratio over 100.[88] The virus is a useful experimental platform because its length, chirality, and binding properties can be adjusted using point mutations of the coat protein. M13 bacteriophage, a naturally-occurring mutant of *fd* bacteriophage, has been used as a scaffold in self-assembling materials.[89,90] In aqueous suspension, *fd* viruses self-assemble into membranes and ribbons in which the chirality, or twist, is expelled to the surface of the assembly (Figure 6.2).[24] The chirality of the viruses in these suspensions can be dynamically and continuously controlled via the temperature of the system, suggesting a new method for manipulating the morphology of nanoscale structures.

Molecular dynamics simulations of mixtures of hard spherocylinders and non-adsorbing depletant molecules produced membranes similar to those found in experiment.[24,91] Because these simulations used simple hard spherocylinders, they could only treat the case of achiral building blocks. These are sufficient to model certain elements of the membrane structure, but they cannot be used to investigate the effect of the building block chirality, and the achiral spherocylinders probably cannot reproduce the ribbon morphology.

6.4 Disks

Some features of the membrane morphology observed in experiments on *fd* virus can be reproduced using a coarse-grained building block and restricting the simulation to two dimensions. In this case, the building block consists of two sites: an isotropic LJ site and a chiral pole. A system of reduced units in which the LJ parameters ϵ_0 and σ_0 are set to unity leaves the three independent parameters of the chiral site: the angle α, the chiral

pole strength μ, and the polar interaction length σ. There are no depletant molecules in these simulations.

These building blocks assemble into finite 2D circular sheets over a wide range of parameter space (Figure 6.3). These sheets are called membranes when their radius is much larger than the size of the building blocks[24] and finite-sized disks in other cases.[92] For $\alpha = 0$, changes in μ and σ alter the spacing between the building blocks but do not affect the hexagonal packing. Because the LJ sites are isotropic, the orientational ordering is determined by the chiral poles alone. In disks that have a single building block at the center, the central pole is perpendicular to the plane of the disk. The building blocks in the first ring around the central pole are all tilted at an angle with respect to the central pole. The second ring is tilted at an angle with respect to the first ring, and so on. The incremental tilt between rings near the center of a large disk is mostly constant, but the incremental tilt increases near the edge of the disk. The incremental tilt near the center increases with α (Figure 6.4), but the tilt at a radius measured as a fraction of the disk radius appears to be insensitive to the number of particles in the disk (Figure 6.5).

If α is small enough or N is large enough so that the poles on the outside ring are tilted by less than or about $\pi/2$ with respect to the central pole, then there is no interruption to the hexagonal packing. If α is large enough so that the poles on the outer ring would be tilted beyond $\pi/2$, then the global minimum is probably no longer a single disk. The tilt angles in Figures 6.3c, 6.3d, and 6.5 that exceed $\pi/2$ would probably not be energetically favorable, since the poles tilted at those angles could form a new, smaller disk. The global minima in these cases appear to consist of several smaller disks associated together, suggesting that this building block can produce the structures treated in depletion-induced phase transition theory.[93]

6.5   Helices and ribbons

Because the *fd* virus has a high aspect ratio, the isotropic LJ site is an inappropriate ingredient in a building block for 3D simulations. A 3D treatment of the chiral viruses must introduce another parameter analogous to the virus length. In the following simulations, the building blocks each consist of a chiral pole and an infinitely-thin rod of length L. The interaction between these rods was LJ-like, and the pairwise energy of two interacting rods was set to

$$4\epsilon_{\mathrm{rod}}\left[\left(\frac{\sigma_{\mathrm{rod}}}{d}\right)^{12} - \left(\frac{\sigma_{\mathrm{rod}}}{d}\right)^{6}\right],\tag{6.3}$$

where d is the distance of closest approach between the two rods as computed using Vega's and Lago's algorithm.[94] Setting the chiral pole length parameters $\sigma_0 = 1$ and the rod
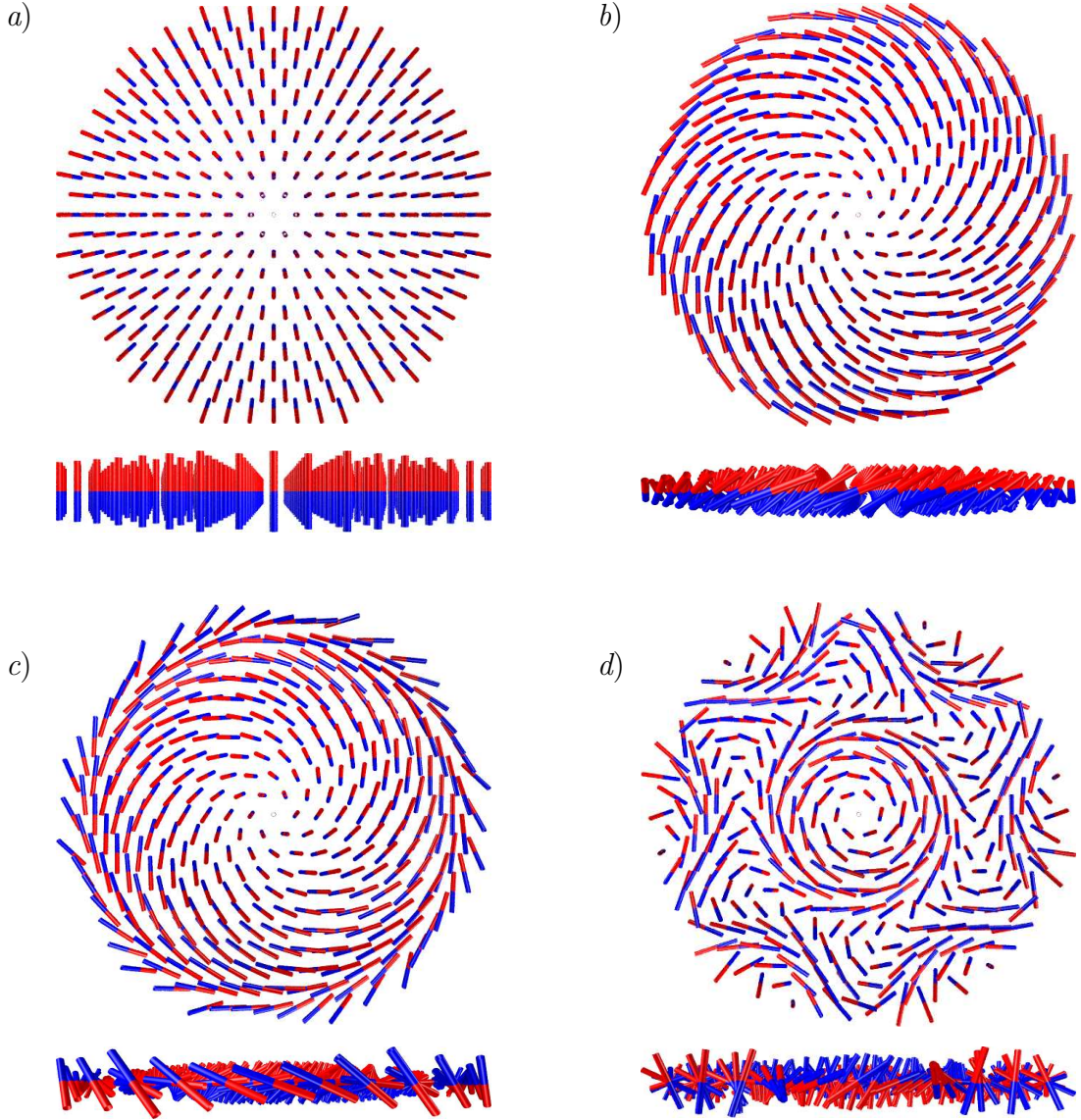
Figure 6.3: Top views (upper panels) and side views (lower panels) of equilibrium disks of 313 chiral pole building blocks restricted to two dimensions. Because the LJ sites in these building blocks are isotropic, the colored rods only indicate the orientation of the chiral pole. The length of the rods is arbitrary. *a)* $\alpha = 0$. The other disks shown were relaxed from starting coordinates very similar to this structure. *b)* $\alpha = 0.5$. *c)* $\alpha = 1.0$. The inner rings are tilted in the same right-handed sense as in the $\alpha = 0.5$ disk, but the outermost ring has tilted beyond $\pi/2$ with respect to the upright center. *d)* $\alpha = 1.25$. A ring about halfway through the disk's radius has tilted beyond $\pi/2$ with respect to the upright center.
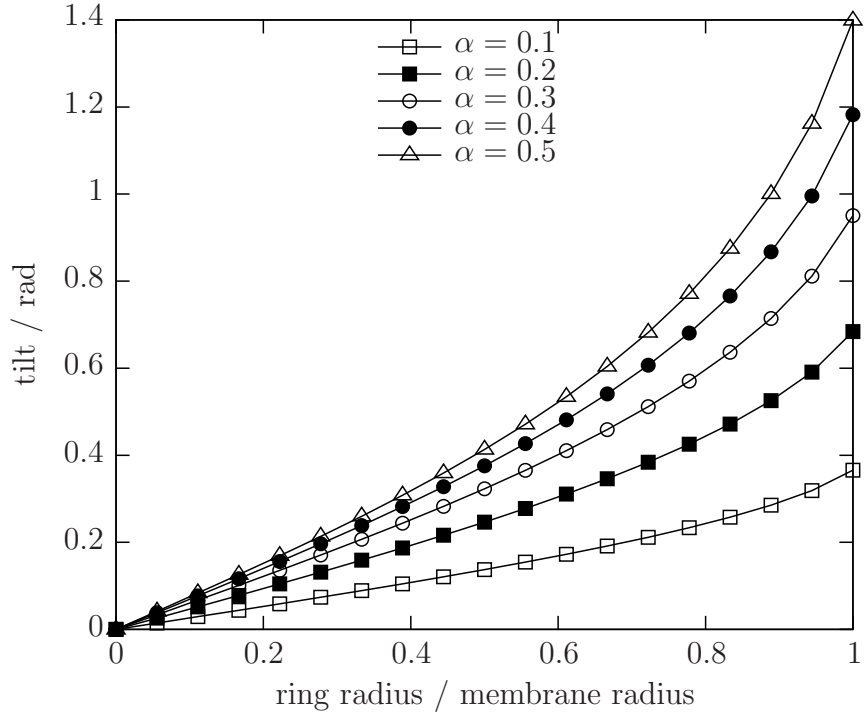
Figure 6.4: The tilt of chiral poles in a disk of 313 chiral pole building blocks restricted to two dimensions. This rate of increase itself increases as the angle α grows. Each line depicts the result of a simulation of a system with a given α. Each point represents the tilt of chiral poles in a given ring in the disk. (Compare with Figure 6.3. The centermost chiral pole is upright and so has zero tilt. Stepping away ring by ring from the center increases the tilt with respect to the center.)

energy $\epsilon_{\mathrm{rod}} = 1$ yields a system of reduced units such that the 3D building block has four free parameters: the angle α, the pole strength μ, and the two rod length scales σ_{rod} and L. Details of the algorithm used to compute d and derivations of the gradients of the potential are provided in Section A.2.

For $\mu \lesssim 1$, the structures of the potential energy minima are mostly determined by the rods and typically consist of isotropic jumbles. The structures of the minima are mostly insensitive to μ when $\mu \gtrsim 1$. Structures with $L \lesssim 1$ approach the $L = 0$ (i.e., isotropic LJ) limit.

For $\mu \gtrsim 1$, the angle α is the most interesting parameter. Building blocks with small α assemble into disks (Figure 6.6). For $L/\sigma_0 \gtrsim 5$, there is one single disk; for smaller L, multiple disks stack on top of one another. For higher α, the building blocks assemble into helices. These helices are themselves composed of very small disks. The competing low-energy minima include a helical 'tape' for the disk and three- and four-way joints for the helix (Figure 6.7).

Finally, equilibrium structures for this building block include a twisted ribbon similar
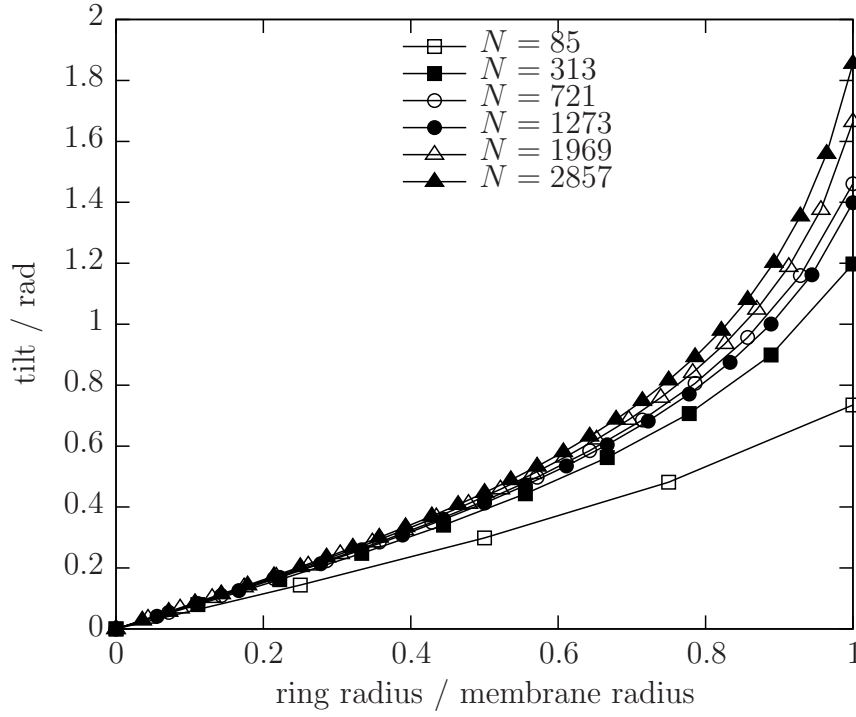
Figure 6.5: The tilt of chiral poles with $\alpha = 0.5$ in disks of varying size. Each line depicts the result of a simulation of an N-particle system. The values for N were chosen so that, for each new N, the radius of the resulting disk would increase by a constant distance. (Compare with Figure 6.3. When the tilt exceeds $\pi/2 \approx 1.6$, the chiral poles are tilted beyond the normal edge seen in 6.3b.)

to those observed in fd virus experiments[24] and predicted by theory[93] (Figure 6.8). These structures can be produced by relaxing from hexagonally-packed rectangles of upright chiral poles similar to the upright disk structure in Figure 6.3a. When viewed from a direction perpendicular to the ribbon's long axis, the ribbon locally resembles a disk: it has the same upright central pole and incremental tilting in the rings of poles surrounding it. The chirality of the interaction between the building blocks induces a right-handed swirl in the plane of the ribbon as well as an overall twist along the long axis of the ribbon.
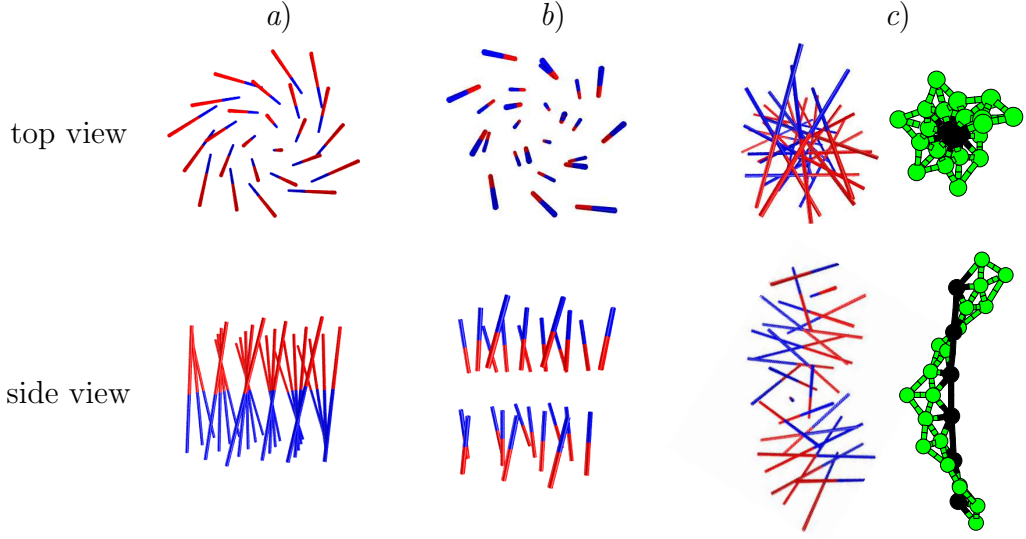
Figure 6.6: Putative global minima for clusters of 25 chiral pole building blocks. Upper panels show top view; lower panels show side views of the same system. In these figures, the length of the depicted rod is equal to L, the length of the building blocks' anisotropic LJ-like rod. a) A single disk ($\alpha = 0.67$, $\mu = 15$, $\sigma_{\text{rod}} = 0.5$, $L = 4$). b) Decreasing the rod length produces two disks ($\alpha = 0.67$, $\mu = 10.25$, $\sigma_{\text{rod}} = 0.5$, $L = 1.3$). c) Increasing the chirality produces a helix ($\alpha = 1.3$, $\mu = 10$, $\sigma_{\text{rod}} = 1$, $L = 4$), which consists of small disks. Each disk has a single upright pole and a surrounding ring of five building blocks. The second representation of the structures has points at the centers of the rods and bonds connecting the centers of nearest neighbors. The difference in color emphasizes the helical structure.
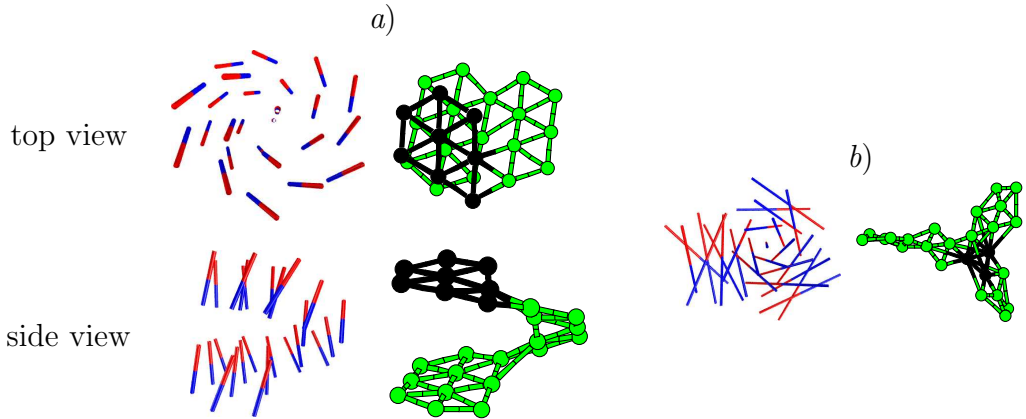
Figure 6.7: Low-lying minima for clusters of 25 chiral pole building blocks. a) Top and side views of a helical tape ($\alpha = 0.67$, $\mu = 10.25$, $\sigma_{\text{rod}} = 0.5$, $L = 1.3$). The difference in color emphasizes different parts of the structure. b) A three-way helix joint ($\alpha = 1.3$, $\mu = 10$, $\sigma_{\text{rod}} = 1$, $L = 4$). The joint is associated with deviations (emphasized in black) from the regular geometry found in the perfect helix.
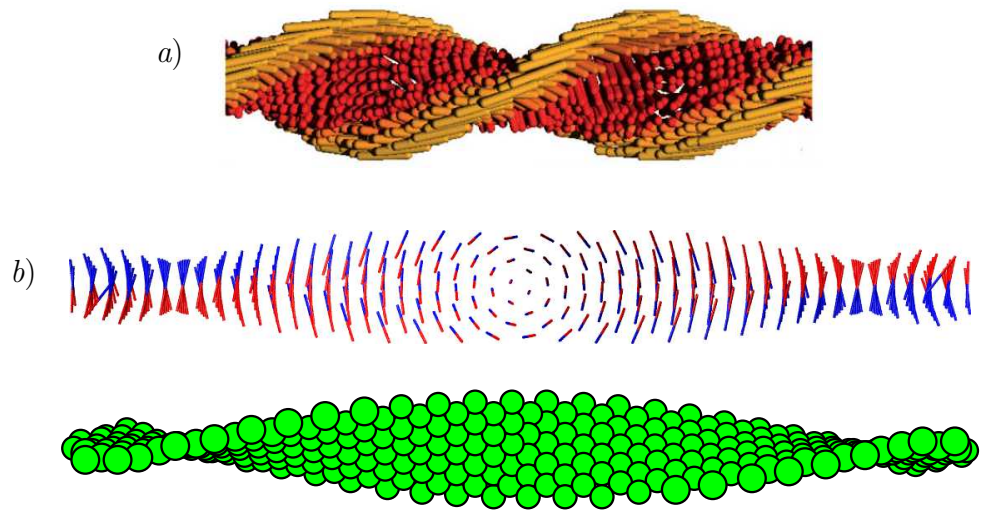
Figure 6.8: *a)* Schematic structure of the twisted ribbons observed in experiment (reproduced from Gibaud et al.[24]). *b)* Two depictions of an equilibrium ribbon structure of chiral pole building blocks ($\alpha = 0.8$, $\mu = 10$, $\sigma_{\mathrm{rod}} = 1$, $L = 2$) relaxed from a hexagonally-packed rectangle 5 building blocks wide and 50 long. Compare the upright poles in the center of the ribbon with the upright rods in the the red regions in *a*, and compare the tilted poles at the left and right ends of the ribbon with the tilted rods in the orange regions in *a*.

Chapter 7

Conclusions and future work

7.1 Conclusions

In this thesis, I proposed and studied five building blocks: the PY bowties in Chapter 4, the two- and four-site PY building blocks in Chapter 5, and the two types of chiral pole building blocks in Chapter 6. Each of these systems has demonstrated some aspect of the relationship between the chirality of a building block and the chirality of the structured formed by assembly of the building blocks. These building blocks might also prove to be useful models of physical systems in their own right.

The PY bowtie is a simple building block with continuously adjustable chirality. Examining single helices of PY bowties showed that the chirality of the helices, measured by their rotation angles Ω, depends on the parameterization of the ellipsoids making up the bowties almost as strongly as on the chirality of the building blocks, measured by their dihedral angle ϕ. For some parameterizations, Ω is nearly proportional to ϕ. In others, positive values ϕ can produce both positive and negative values Ω. This discovery may provide some insight into the ambiguous relationship between building block and structure chiralities.

The four-site building block, though achiral, assembled into chiral screw-like structures. One set of screw-like structures provided a demonstration of the compatibility of certain sets of chiral structures.

I used the novel, coarse-grained chiral polar potential two construct building blocks for 2D and 3D simulations. The chiral polar potential favors geometries in which adjacent building blocks are at a specified but adjustable angle with respect to one another. This potential therefore favors chiral structures whose chirality can be continuously adjusted. These simulations produced a variety of morphologies, including chiral disks, helices, and ribbons. These assemblies closely resemble structures found in experimental studies of a

chiral rod-like virus.

7.2 Future work

Having observed a possibly novel relationship between the chirality of building blocks and their assembled structures in simulations of the PY bowties, it is important to see if a comparable physical system, like an anisotropic colloid, can be made to exhibit this type of behavior. An experimental collaboration with members of the Melville Laboratory for Polymer Synthesis is planned. I am also interested in pursuing simulations of assemblies of proteins whose chiralities switch when a single residue is mutated. These changes in structure chirality might be usefully compared with changes of building block parameterization rather than switches in building block chirality. More computationally expensive simulations using the original building block could also help clarify the relationship between the number of building blocks and the length of the helices at the bottom of the main funnel on the PES.

A four-site PY building block, whether chiral or achiral, should be able to reproduce more complicated structures that demonstrate the steric compatibility of sets of chiral structures beyond what has already been found.

The chiral polar potential can be used to add chiral interactions to any building block. Previous simulations of the *fd* viruses used achiral spherocylinders and depletant molecules to reproduce the entropic forces that cause the assembled structures to exhibit chirality. By adding the chiral pole to this building block, I should be able to reproduce the complementarity of energetic and entropic chiral forces observed in experiment and measure observables like line tension and twist penetration depth. The chiral pole potential might also be useful for modeling biological structures with chiral building blocks. For example, blood clots are assemblies of fibers in turn assembled from chiral rod-like building blocks.[95]

Overall, I hope that this thesis has demonstrated some new principles that will help unravel the relation between building block and assembly chiralities. I also hope that it has provided some new simulation tools and building blocks that will advance future studies of chiral assemblies.

Appendix A

Gradients for potentials in Chapter 6

A.1 Chiral pole

The potential is

$$U = -\frac{\mu^2 \sigma^3}{r^3} \left[\cos \alpha \left(\hat{\boldsymbol{\mu}}^i \cdot \hat{\boldsymbol{\mu}}^j \right) + \sin \alpha \left(\hat{\boldsymbol{\mu}}^i \times \hat{\boldsymbol{\mu}}^j \right) \cdot \hat{\boldsymbol{r}} \right], \tag{A.1}$$

where $\boldsymbol{\mu}^i$ and $\boldsymbol{\mu}^j$ are the poles, $|\boldsymbol{\mu}^i| = |\boldsymbol{\mu}^j| = \mu$ is the pole strength, σ is the interaction length scale, and $\boldsymbol{r}$ is the vector separating the sites.

Noting that

$$\frac{\partial}{\partial \boldsymbol{r}} \left(\boldsymbol{a} \cdot \hat{\boldsymbol{r}} \right) = \frac{1}{r} \left[\boldsymbol{a} - \left(\boldsymbol{a} \cdot \hat{\boldsymbol{r}} \right) \hat{\boldsymbol{r}} \right], \tag{A.2}$$

where $\boldsymbol{a}$ is constant, the radial gradient is

$$\frac{\mathrm{d}U}{\mathrm{d}\boldsymbol{r}^i} = -\frac{\mu^2 \sigma^3}{r^4} \left\{ \cos \alpha \left[-3 \left(\hat{\boldsymbol{\mu}}^i \cdot \hat{\boldsymbol{\mu}}^j \right) \hat{\boldsymbol{r}} \right] + \sin \alpha \left[\left(\hat{\boldsymbol{\mu}}^i \times \hat{\boldsymbol{\mu}}^j \right) - 4 \left(\hat{\boldsymbol{\mu}}^i \times \hat{\boldsymbol{\mu}}^j \cdot \hat{\boldsymbol{r}} \right) \hat{\boldsymbol{r}} \right] \right\}. \tag{A.3}$$

To compute the angular gradients, first note that

$$\hat{\boldsymbol{\mu}}^i = \boldsymbol{R}^I \hat{\boldsymbol{\mu}}^{i0} \equiv \boldsymbol{R}^I \left(\boldsymbol{R}^{i0} \hat{\boldsymbol{z}} \right) \tag{A.4}$$

so that

$$\frac{\mathrm{d}U}{\mathrm{d}p_k^I} = -\frac{\mu^2}{r^3} \left\{ \cos \alpha \left[\left(\boldsymbol{R}_k^I \hat{\boldsymbol{\mu}}^{i0} \right) \cdot \hat{\boldsymbol{\mu}}^j \right] + \sin \alpha \left[\left(\boldsymbol{R}_k^I \hat{\boldsymbol{\mu}}^{i0} \right) \times \hat{\boldsymbol{\mu}}^j \right] \cdot \hat{\boldsymbol{r}} \right\} \tag{A.5}$$

$$\frac{\mathrm{d}U}{\mathrm{d}p_k^J} = -\frac{\mu^2}{r^3} \left\{ \cos \alpha \left[\hat{\boldsymbol{\mu}}^i \cdot \left(\boldsymbol{R}_k^J \hat{\boldsymbol{\mu}}^{j0} \right) \right] + \sin \alpha \left[\hat{\boldsymbol{\mu}}^i \times \left(\boldsymbol{R}_k^J \hat{\boldsymbol{\mu}}^{j0} \right) \right] \cdot \hat{\boldsymbol{r}} \right\}. \tag{A.6}$$

A.2   Lennard-Jones-like infinitely-thin rod

In the PY potential, a LJ-like interaction is modulated by the distance of closest approach between two ellipsoids. In the rod potential, a LJ-like interaction is modulated by the distance of closest approach between two rods. In this way, the rod potential is a limiting case of a spherocylinder potential where the cylinder radius approaches zero.

Two rods of lengths L^i and L^j centered at $\boldsymbol{r}^i$ and $\boldsymbol{r}^j$ with orientations defined by their poles $\hat{\boldsymbol{\mu}}^i$ and $\hat{\boldsymbol{\mu}}^j$ have a distance of closest approach

$$d = \min_{\boldsymbol{x}^i \in S^i, \boldsymbol{x}^j \in S^j} \left| \boldsymbol{x}^i - \boldsymbol{x}^j \right|, \tag{A.7}$$

where S^i is the set of all the points in rod i. It is convenient to write the points of closest approach $\boldsymbol{x}^i$ and $\boldsymbol{x}^j$ as

$$\boldsymbol{x}^i = \boldsymbol{r}^i - \lambda^i \hat{\boldsymbol{\mu}}^i, \tag{A.8}$$

where $\lambda^i \leq |L^i/2|$. Thus,

$$d = \min_{\lambda^i \leq |L^i/2|, \lambda^j \leq |L^j/2|} \left| \boldsymbol{r}^{ij} - \lambda^i \hat{\boldsymbol{\mu}}^i + \lambda^j \hat{\boldsymbol{\mu}}^j \right|. \tag{A.9}$$

The pairwise energy is

$$U^{ij} = 4\epsilon_0 \left[\left(\frac{\sigma_{\text{rod}}}{d} \right)^{12} - \left(\frac{\sigma_{\text{rod}}}{d} \right)^6 \right]. \tag{A.10}$$

The λ values are necessary for computing the energy and gradient. There is a deterministic algorithm for finding λ^i and λ^j.[94] The algorithm is roughly:

1. Check if $\hat{\boldsymbol{\mu}}^i$ is parallel to $\hat{\boldsymbol{\mu}}^j$. If the rods are parallel and exactly side-by-side, set $\lambda^i = \lambda^j = 0$. If the two rods are parallel but not side-by-side, set $\lambda^i = \pm L^i/2$, where the sign is the one that places $\boldsymbol{x}^i$ nearer the interior of the other rod, and set λ^j to the value that chooses the correct contact point in S^j.

2. If the two rods are not parallel, compute

$$\lambda^i = \left[1 - \left(\hat{\boldsymbol{\mu}}^i \cdot \hat{\boldsymbol{\mu}}^j \right)^2 \right]^{-1} \left[\boldsymbol{r} \cdot \hat{\boldsymbol{\mu}}^i - \left(\hat{\boldsymbol{\mu}}^i \cdot \hat{\boldsymbol{\mu}}^j \right) \left(\boldsymbol{r}^{ij} \cdot \hat{\boldsymbol{\mu}}^j \right) \right] \tag{A.11}$$

$$\lambda^j = \left[1 - \left(\hat{\boldsymbol{\mu}}^i \cdot \hat{\boldsymbol{\mu}}^j \right)^2 \right]^{-1} \left[-\boldsymbol{r} \cdot \hat{\boldsymbol{\mu}}^j + \left(\hat{\boldsymbol{\mu}}^i \cdot \hat{\boldsymbol{\mu}}^j \right) \left(\boldsymbol{r}^{ij} \cdot \hat{\boldsymbol{\mu}}^i \right) \right] \tag{A.12}$$

3. If λ^i is outside of the permitted range, change it to the closest of the two values $\pm L^i/2$. Recompute λ^j using this λ^i as input.

4. If λ^j is outside of the permitted range, change it to the closest of the two values

$\pm L^j/2$. Recompute λ^i using this λ^j as input. If λ^i is still outside the permitted range, change it to the closest endpoint.

5. Compute d^2.

It is easier to compute and take the derivatives of $\delta \equiv d^2$ rather than d. In these terms, the pairwise interaction is

$$U^{ij} = 4\epsilon_0 \left[\delta^{-6} - \delta^{-3} \right]. \tag{A.13}$$

The translational derivatives are

$$\frac{\mathrm{d}U^{ij}}{\mathrm{d}\boldsymbol{r}^i} = 4\epsilon_0 \left[-6\delta^{-7} + 3\delta^{-4} \right] \frac{\mathrm{d}\delta}{\mathrm{d}\boldsymbol{r}^i} \tag{A.14}$$

$$\frac{\mathrm{d}\delta}{\mathrm{d}\boldsymbol{r}^i} = \frac{\partial\delta}{\partial\boldsymbol{r}^i} + \frac{\partial\lambda^i}{\partial\boldsymbol{r}^i}\frac{\partial\delta}{\partial\lambda^i} + \frac{\partial\lambda^j}{\partial\boldsymbol{r}^i}\frac{\partial\delta}{\partial\lambda^j} \tag{A.15}$$

$$\frac{\partial\delta}{\partial\boldsymbol{r}^i} = 2\left(\boldsymbol{r}^{ij} - \lambda^i\hat{\boldsymbol{\mu}}^i + \lambda^j\hat{\boldsymbol{\mu}}^j \right) \tag{A.16}$$

where

$$\frac{\partial\lambda^i}{\partial\boldsymbol{r}^i} = \begin{cases} \left[1 - \left(\hat{\boldsymbol{\mu}}^i \cdot \hat{\boldsymbol{\mu}}^j\right)^2\right]^{-1} \left[\hat{\boldsymbol{\mu}}^i - \left(\hat{\boldsymbol{\mu}}^i \cdot \hat{\boldsymbol{\mu}}^j\right)\hat{\boldsymbol{\mu}}^j\right] & \text{if } \lambda^i \neq \pm L^i/2 \\ 0 & \text{if } \lambda^i = \pm L^i/2 \end{cases} \tag{A.17}$$

$$\frac{\partial\delta}{\partial\lambda^i} = -2\left[\left(\boldsymbol{r}^{ij} \cdot \hat{\boldsymbol{\mu}}^i\right) - \lambda^i + \lambda^j\left(\hat{\boldsymbol{\mu}}^i \cdot \hat{\boldsymbol{\mu}}^j\right) \right] \tag{A.18}$$

$$\frac{\partial\lambda^j}{\partial\boldsymbol{r}^i} = \begin{cases} \left[1 - \left(\hat{\boldsymbol{\mu}}^i \cdot \hat{\boldsymbol{\mu}}^j\right)^2\right]^{-1} \left[-\hat{\boldsymbol{\mu}}^j + \left(\hat{\boldsymbol{\mu}}^i \cdot \hat{\boldsymbol{\mu}}^j\right)\hat{\boldsymbol{\mu}}^i\right] & \text{if } \lambda^j \neq \pm L^j/2 \\ 0 & \text{if } \lambda^j = \pm L^j/2 \end{cases} \tag{A.19}$$

$$\frac{\partial\delta}{\partial\lambda^j} = -2\left[\left(\boldsymbol{r}^{ij} \cdot \hat{\boldsymbol{\mu}}^j\right) - \lambda^i\left(\hat{\boldsymbol{\mu}}^i \cdot \hat{\boldsymbol{\mu}}^j\right) + \lambda^j \right] \tag{A.20}$$

As usual, $\mathrm{d}U^{ij}/\mathrm{d}\boldsymbol{r}^j = -\mathrm{d}U^{ij}/\mathrm{d}\boldsymbol{r}^i$.

The orientational derivatives are

$$\frac{\mathrm{d}U^{ij}}{\mathrm{d}p_k^i} = 4\epsilon_0 \left[-6\delta^{-7} + 3\delta^{-4} \right] \frac{\mathrm{d}\delta}{\mathrm{d}p_k^i} \tag{A.21}$$

$$\frac{\mathrm{d}\delta}{\mathrm{d}p_k^i} = \frac{\partial\delta}{\partial p_k^i} + \frac{\partial\lambda^i}{\partial p_k^i}\frac{\partial\delta}{\partial\lambda^i} + \frac{\partial\lambda^j}{\partial p_k^i}\frac{\partial\delta}{\partial\lambda^j} \tag{A.22}$$

$$\frac{\partial\delta}{\partial p_k^i} = -2\lambda^i \left(\boldsymbol{R}_k^I \hat{\boldsymbol{\mu}}^{i0} \right) \cdot \boldsymbol{x}^{ij} \tag{A.23}$$

where

$$\frac{\partial \lambda^i}{\partial p_k^i} = 2 \left[1 - \left(\hat{\boldsymbol{\mu}}^i \cdot \hat{\boldsymbol{\mu}}^j \right)^2 \right]^{-2} \left(\hat{\boldsymbol{\mu}}^i \cdot \hat{\boldsymbol{\mu}}^j \right) \left(\boldsymbol{R}_k^I \hat{\boldsymbol{\mu}}^{i0} \cdot \hat{\boldsymbol{\mu}}^j \right) \left[\boldsymbol{r}^{ij} \cdot \hat{\boldsymbol{\mu}}^i - \left(\hat{\boldsymbol{\mu}}^i \cdot \hat{\boldsymbol{\mu}}^j \right) \left(\boldsymbol{r}^{ij} \cdot \hat{\boldsymbol{\mu}}^j \right) \right]$$
$$+ \left[1 - \left(\hat{\boldsymbol{\mu}}^i \cdot \hat{\boldsymbol{\mu}}^j \right)^2 \right]^{-1} \left[\boldsymbol{r}^{ij} \cdot \boldsymbol{R}_k^I \hat{\boldsymbol{\mu}}^{i0} - \left(\boldsymbol{R}_k^I \hat{\boldsymbol{\mu}}^{i0} \cdot \hat{\boldsymbol{\mu}}^j \right) \left(\boldsymbol{r}^{ij} \cdot \hat{\boldsymbol{\mu}}^j \right) \right] \quad \text{(A.24)}$$

$$\frac{\partial \lambda^j}{\partial p_k^i} = 2 \left[1 - \left(\hat{\boldsymbol{\mu}}^i \cdot \hat{\boldsymbol{\mu}}^j \right)^2 \right]^{-2} \left(\hat{\boldsymbol{\mu}}^i \cdot \hat{\boldsymbol{\mu}}^j \right) \left(\boldsymbol{R}_k^I \hat{\boldsymbol{\mu}}^{i0} \cdot \hat{\boldsymbol{\mu}}^j \right) \left[-\boldsymbol{r}^{ij} \cdot \hat{\boldsymbol{\mu}}^j + \left(\hat{\boldsymbol{\mu}}^i \cdot \hat{\boldsymbol{\mu}}^j \right) \left(\boldsymbol{r}^{ij} \cdot \hat{\boldsymbol{\mu}}^i \right) \right]$$
$$+ \left[1 - \left(\hat{\boldsymbol{\mu}}^i \cdot \hat{\boldsymbol{\mu}}^j \right)^2 \right]^{-1} \left[\left(\boldsymbol{R}_k^I \hat{\boldsymbol{\mu}}^{i0} \cdot \hat{\boldsymbol{\mu}}^j \right) \left(\boldsymbol{r}^{ij} \cdot \hat{\boldsymbol{\mu}}^i \right) - \left(\hat{\boldsymbol{\mu}}^i \cdot \hat{\boldsymbol{\mu}}^j \right) \left(\boldsymbol{r}^{ij} \cdot \boldsymbol{R}_k^I \hat{\boldsymbol{\mu}}^{i0} \right) \right] \quad \text{(A.25)}$$

$$\frac{\partial \delta}{\partial p_k^i} = -2\lambda^j \left(\boldsymbol{R}_k^J \hat{\boldsymbol{\mu}}^{j0} \right) \cdot \boldsymbol{x}^{ij} \quad \text{(A.26)}$$

$$\frac{\partial \lambda^i}{\partial p_k^i} = 2 \left[1 - \left(\hat{\boldsymbol{\mu}}^i \cdot \hat{\boldsymbol{\mu}}^j \right)^2 \right]^{-2} \left(\hat{\boldsymbol{\mu}}^i \cdot \hat{\boldsymbol{\mu}}^j \right) \left(\hat{\boldsymbol{\mu}}^i \cdot \boldsymbol{R}_k^J \hat{\boldsymbol{\mu}}^{j0} \right) \left[\boldsymbol{r}^{ij} \cdot \hat{\boldsymbol{\mu}}^i - \left(\hat{\boldsymbol{\mu}}^i \cdot \hat{\boldsymbol{\mu}}^j \right) \left(\boldsymbol{r}^{ij} \cdot \hat{\boldsymbol{\mu}}^j \right) \right]$$
$$- \left[1 - \left(\hat{\boldsymbol{\mu}}^i \cdot \hat{\boldsymbol{\mu}}^j \right)^2 \right]^{-1} \left[\left(\hat{\boldsymbol{\mu}}^i \cdot \boldsymbol{R}_k^J \hat{\boldsymbol{\mu}}^{j0} \right) \left(\boldsymbol{r}^{ij} \cdot \hat{\boldsymbol{\mu}}^j \right) + \left(\hat{\boldsymbol{\mu}}^i \cdot \hat{\boldsymbol{\mu}}^j \right) \left(\boldsymbol{r}^{ij} \cdot \boldsymbol{R}_k^J \hat{\boldsymbol{\mu}}^j \right) \right] \quad \text{(A.27)}$$

$$\frac{\partial \lambda^j}{\partial p_k^j} = 2 \left[1 - \left(\hat{\boldsymbol{\mu}}^i \cdot \hat{\boldsymbol{\mu}}^j \right)^2 \right]^{-2} \left(\hat{\boldsymbol{\mu}}^i \cdot \hat{\boldsymbol{\mu}}^j \right) \left(\hat{\boldsymbol{\mu}}^i \cdot \boldsymbol{R}_k^J \hat{\boldsymbol{\mu}}^{j0} \right) \left[-\boldsymbol{r}^{ij} \cdot \hat{\boldsymbol{\mu}}^j + \left(\hat{\boldsymbol{\mu}}^i \cdot \hat{\boldsymbol{\mu}}^j \right) \left(\boldsymbol{r}^{ij} \cdot \hat{\boldsymbol{\mu}}^i \right) \right]$$
$$+ \left[1 - \left(\hat{\boldsymbol{\mu}}^i \cdot \hat{\boldsymbol{\mu}}^j \right)^2 \right]^{-1} \left[-\left(\boldsymbol{r}^{ij} \cdot \boldsymbol{R}_k^J \hat{\boldsymbol{\mu}}^{j0} \right) + \left(\hat{\boldsymbol{\mu}}^i \cdot \boldsymbol{R}_k^J \hat{\boldsymbol{\mu}}^{j0} \right) \left(\boldsymbol{r}^{ij} \cdot \hat{\boldsymbol{\mu}}^{i0} \right) \right] \quad \text{(A.28)}$$

Bibliography

[1] G. M. Whitesides and B. Grzybowski, Science **295**, 2418 (2002).

[2] W. A. Lopes and H. M. Jaeger, Nature **414**, 735 (2001).

[3] I. W. Hamley, Angew. Chem. Int. Ed. **42**, 16921712 (2003).

[4] S. Zhang, Nat. Biotechnol. **21**, 1171 (2003).

[5] B. A. Grzybowski, C. E. Wilmer, J. Kim, K. P. Browne and K. J. M. Bishop, Soft Matter **5**, 1110 (2009).

[6] G. M. Whitesides, J. P. Mathias and C. T. Seto, Science **254**, 1312 (1991).

[7] C. T. Black, C. B. Murray, R. L. Sandstrom and S. Sun, Science **290**, 1131 (2000).

[8] M. Lazzari and M. López-Quintela, Adv. Mater. **15**, 1583 (2003).

[9] K. T. Nam, D. Kim, P. J. Yoo, C. Chiang, N. Meethong, P. T. Hammond, Y. Chiang and A. M. Belcher, Science **312**, 885 (2006).

[10] D. Frenkel and B. Smit, *Understanding Molecular Simulation*, Academic Press (2001).

[11] D. G. Grier, Nature **424**, 810 (2003).

[12] K. E. Strecker, G. B. Partridge, A. G. Truscott and R. G. Hulet, Nature **417**, 150 (2002).

[13] Y. Sugimoto, P. Pou, M. Abe, P. Jelinek, R. Pérez, S. Morita and O. Custance, Nature **446**, 64 (2007).

[14] J. Gay and B. Berne, J. Chem. Phys. **74**, 3316 (1981).

[15] D. Frenkel, H. N. W. Lekkerkerker and A. Stroobants, Nature **332**, 822 (1988).

[16] E. Meijer and D. Frenkel, J. Chem. Phys. **100**, 6873 (1994).

[17] W. C. K. Poon, J. Phys.-Condens. Mat. **14**, R859 (2002).

[18] W. W. Wood and F. R. Parker, J. Chem. Phys. **27**, 720 (1957).

[19] S. C. Glotzer and M. J. Solomon, Nat. Mater. **6**, 557 (2007).

[20] S. Fejer, *Self-assembly in complex systems*, Ph.D. thesis, University of Cambridge (2009).

[21] A. B. Harris, R. D. Kamien and T. C. Lubensky, Rev. Mod. Phys. **71**, 1745 (1999).

[22] A. Aggeli, I. A. Nyrkova, M. Bell, R. Harding, L. Carrick, T. C. B. McLeish, A. N. Semenov and N. Boden, Proc. Nat. Acad. Sci. USA **98**, 11857 (2001).

[23] Y. Yang, R. B. Meyer and M. F. Hagan, Phys. Rev. Lett. **104**, 258102 (2010).

[24] T. Gibaud, E. Barry, M. J. Zakhary, M. Henglin, A. Ward, Y. Yang, C. Berciu, R. Oldenbourg, M. F. Hagan, D. Nicastro, R. B. Meyer and Z. Dogic, Nature **481**, 348 (2012).

[25] L. Paramonov and S. N. Yaliraki, J. Chem. Phys. **123**, 194111 (2005).

[26] J. N. Murrell and K. J. Laidler, T. Faraday Soc. **64**, 371 (1968).

[27] D. J. Wales, *Energy Landscapes*, Cambridge University Press (2003).

[28] J. W. Perram and M. Wertheim, J. Comp. Phys. **58**, 409 (1985).

[29] J. W. Perram, J. Rasmussen, E. Præstgaard and J. L. Lebowitz, Phys. Rev. E **54**, 6565 (1996).

[30] S. N. Fejer and D. J. Wales, Phys. Rev. Lett. **99**, 086106 (2007).

[31] R. Fletcher, *Practical Methods of Optimization*, Wiley (2000).

[32] L. E. Scales, *Introduction to non-linear optimization*, Springer-Verlag (1985).

[33] D. J. Wales, J. Chem. Phys. **101**, 3750 (1994).

[34] J. Nocedal, Math. Comput. **35**, 773 (1980).

[35] D. C. Liu and J. Nocedal, Math. Program. **45**, 503 (1989).

[36] D. J. Wales, Mol. Phys. **100**, 3285 (2002).

[37] J. Barzilai and J. M. Borwein, IMA J. Numer. Anal. **8**, 141 (1988).

[38] M. Raydan, SIAM J. Optimiz. **7**, 26 (1997).

[39] J. K. Lee, J. A. Barker and F. F. Abraham, J. Chem. Phys. **58**, 3166 (1973).

[40] M. R. Hoare and J. McInnes, Faraday Discuss. Chem. S. **61**, 12 (1976).

[41] A. Törn and A. Žilinskas, *Global Optimization*, Springer (1989).

[42] L. T. Wille and J. Vennik, J. Phys. A-Math. Gen. **18**, L419 (1985).

[43] S. Forrest, Science **261**, 872 (1993).

[44] S. Kirkpatrick, C. D. Gelatt and M. P. Vecchi, Science **220**, 671 (1983).

[45] F. Glover, ORSA J. Comput. **1**, 190 (1989).

[46] F. Glover, ORSA J. Comput. **2**, 4 (1990).

[47] U. H. E. Hansmann and L. T. Wille, Phys. Rev. Lett. **88**, 068105 (2002).

[48] F. H. Stillinger and T. A. Weber, J. Stat. Phys. **52**, 1429 (1988).

[49] L. Piela, J. Kostrowicki and H. A. Scheraga, J. Phys. Chem. **93**, 3339 (1989).

[50] D. J. Wales and J. P. K. Doye, J. Phys. Chem. A **101**, 5111 (1997).

[51] D. J. Wales and H. A. Scheraga, Science **285**, 1368 (1999).

[52] N. Metropolis, A. W. Rosenbluth, M. N. Rosenbluth, A. H. Teller and E. Teller, J. Chem. Phys. **21**, 1087 (1953).

[53] *GMIN: a program for basin-hopping global optimisation*, http://www-wales.ch.cam.ac.uk/gmin.

[54] O. M. Becker and M. Karplus, J. Chem. Phys. **106**, 1495 (1997).

[55] D. J. Wales, M. A. Miller and T. R. Walsh, Nature **394**, 758 (1998).

[56] D. J. Wales and R. S. Berry, J. Chem. Soc. Faraday T. **88**, 543 (1992).

[57] *OPTIM: a program for geometry optimisation and pathway calculations*, http://www-wales.ch.cam.ac.uk/optim.

[58] *PATHSAMPLE: a program for generating connected stationary point databases and extracting global kinetics*, http://www-wales.ch.cam.ac.uk/pathsample.

[59] R. P. Brent, *Algorithms for Minimization Without Derivatives*, Courier Dover (2002).

[60] S. D. Stoddard and J. Ford, Phys. Rev. A **8**, 1504 (1973).

[61] D. Chakrabarti and D. Wales, Phys. Chem. Chem. Phys. **11**, 1970 (2009).

[62] L. J. Lewis and G. Wahnström, Phys. Rev. E **50**, 3865 (1994).

[63] M. A. Miller and D. J. Wales, J. Phys. Chem. B **109**, 23109 (2005).

[64] M. J. Stevens and G. S. Grest, Phys. Rev. E **51**, 5976 (1995).

[65] D. Chakrabarti, S. N. Fejer and D. J. Wales, Proc. Nat. Acad. Sci. USA **106**, 20164 (2009).

[66] S. N. Fejer, D. Chakrabarti and D. J. Wales, ACS Nano **4**, 219 (2010).

[67] S. N. Fejer, D. Chakrabarti and D. J. Wales, Soft Matter **7**, 3553 (2011).

[68] T. E. Ouldridge, I. G. Johnston, A. A. Louis and J. P. K. Doye, J. Chem. Phys. **130**, 065101 (2009).

[69] N. Rubin, E. Perugia, S. G. Wolf, E. Klein, M. Fridkin and L. Addadi, J. Am. Chem. Soc. **132**, 4242 (2010).

[70] N. Rubin, E. Perugia, M. Goldschmidt, M. Fridkin and L. Addadi, J. Am. Chem. Soc. **130**, 4602 (2008).

[71] W. Dzwolak, A. Loksztejn, A. Galinska-Rakoczy, R. Adachi, Y. Goto and L. Rupnicki, J. Am. Chem. Soc. **129**, 7517 (2007).

[72] A. Loksztejn and W. Dzwolak, J. Mol. Biol. **379**, 9 (2008).

[73] B. N. Thomas, C. M. Lindemann and N. A. Clark, Phys. Rev. E **59**, 3040 (1999).

[74] H. Lichtenegger, M. Mller, O. Paris, C. Riekel and P. Fratzl, J. Appl. Crystallogr. **32**, 1127 (1999).

[75] F. Frank, Biochim. Biophys. Acta **11**, 459 (1953).

[76] V. Avetisov and V. Goldanskii, Proc. Nat. Acad. Sci. USA **93**, 11435 (1996).

[77] T. Buhse, D. Durand, D. Kondepudi, J. Laudadio and S. Spilker, Phys. Rev. Lett. **84**, 4405 (2000).

[78] D. K. Kondepudi and K. Asakura, Acc. Chem. Res. **34**, 946 (2001).

[79] L. Li, H. Jiang, B. Messmore, S. Bull and S. Stupp, Angew. Chem. **119**, 5977 (2007).

[80] K. S. Cheon, J. V. Selinger and M. M. Green, Angew. Chem. Int. Ed. **39**, 14821485 (2000).

[81] K. Tang, M. M. Green, K. S. Cheon, J. V. Selinger and B. A. Garetz, J. Am. Chem. Soc. **125**, 7313 (2003).

[82] Z. Li and H. A. Scheraga, Proc. Nat. Acad. Sci. USA **84**, 6611 (1987).

[83] J. P. K. Doye, M. A. Miller and D. J. Wales, J. Chem. Phys. **110**, 6896 (1999).

[84] J. P. K. Doye and D. J. Wales, J. Chem. Phys. **116**, 3777 (2002).

[85] J. Lehn, *Supramolecular Chemistry*, Wiley-VCH (1995).

[86] H. Engelkamp, S. Middelbeek, R. J. M. and Nolte, Science **284**, 785 (1999).

[87] E. Barry, D. Beller and Z. Dogic, Soft Matter (2009).

[88] Z. Dogic and S. Fraden, Curr. Opin. Colloid In. **11**, 47 (2006).

[89] Y. J. Lee, H. Yi, W. Kim, K. Kang, D. S. Yun, M. S. Strano, G. Ceder and A. M. Belcher, Science **324**, 1051 (2009).

[90] X. Dang, H. Yi, M. Ham, J. Qi, D. S. Yun, R. Ladewski, M. S. Strano, P. T. Hammond and A. M. Belcher, Nat. Nanotechnol. **6**, 377 (2011).

[91] Y. Yang, E. Barry, Z. Dogic and M. F. Hagan, Soft Matter **8**, 707 (2012).

[92] R. A. Pelcovits and R. B. Meyer, Liq. Cryst. **36**, 1157 (2009).

[93] C. N. Kaplan, H. Tu, R. A. Pelcovits and R. B. Meyer, Phys. Rev. E **82**, 021701 (2010).

[94] C. Vega and S. Lago, Comput. Chem. **18**, 55 (1994).

[95] J. W. Weisel, C. Nagaswami and L. Makowski, Proc. Nat. Acad. Sci. USA **84**, 8991 (1987).